Journal of Computational Physics 537 (2025) 114111

Contents lists available at ScienceDirect

Journal of Computational Physics

journal homepage: www.elsevier.com/locate/jcp

The Hermite-Taylor correction function method for embedded boundary and Maxwell's interface problems

Yann-Meing Law [a,*], Daniel Appelö [b], Thomas Hagstrom [c]

[a] Department of Mathematics and Industrial Engineering, Polytechnique Montréal, C.P. 6079, succ. Centre-ville, Montréal, QC H3C 3A7, Canada
[b] Department of Mathematics, Virginia Tech, 24060, Blacksburg, VA, USA
[c] Department of Mathematics, Southern Methodist University, 75275, Dallas, TX, USA

ARTICLE INFO

2000 MSC:
35Q61
65M70
78A45

Keywords:
Hermite method
Correction function method
Maxwell's equations
High order
Embedded boundary conditions
Interface conditions

ABSTRACT

We propose a novel Hermite-Taylor correction function method to handle embedded boundary and interface conditions for Maxwell's equations. The Hermite-Taylor method evolves the electromagnetic fields and their derivatives through order m in each Cartesian coordinate. This makes the development of a systematic approach to enforce boundary and interface conditions difficult. Here we use the correction function method to update the numerical solution where the Hermite-Taylor method cannot be applied directly. Time derivatives of boundary and interface conditions, converted into spatial derivatives, are enforced to obtain a stable method and relax the time-step size restriction of the Hermite-Taylor correction function method. The proposed high-order method offers a flexible systematic approach to handle embedded boundary and interface problems, including problems with discontinuous solutions at the interface. This method is also easily adaptable to other first order hyperbolic systems.

1. Introduction

Interface and boundary problems are of great importance in electromagnetics. The former type of problem involves interfaces between different media and is found in many applications in electromechanics, biophotonics and magneto-hydrodynamics, to name a few. The latter type of problem focuses on the interaction between the electromagnetic fields and a surface, and is found in waveguide applications.

In computational electromagnetics, many challenges arise from those types of problems. The development of efficient high-order methods are important to diminish the phase error for long time simulations [1]. This is particularly difficult for interface problems where the solution can be discontinuous at the interface. In addition to high-order accuracy, a numerical method should also be able to handle complex geometries. Many high-order numerical methods have been developed to handle Maxwell's interface and boundary problems, such as finite-difference time-domain (FDTD) methods [2–7], discontinuous Galerkin (DG) methods [8,9] and pseudo-spectral methods [10–13].

In this work, we focus on the Hermite-Taylor method, introduced by Goodrich, Hagstrom and Lorenz in 2005 [14]. This high-order method is particularly well-suited for linear hyperbolic problems with periodic boundary conditions. By evolving in time the variables and their derivatives through order m in each coordinate, the Hermite-Taylor method achieves a $(2m+1)$ rate of convergence. The stability condition of this method depends only on the largest wave speed of the problem and is independent of the order of accuracy, making the Hermite-Taylor method appealing for large scale problems.

* Corresponding author.
E-mail addresses: yann-meing.law@polymtl.ca (Y.-M. Law), appelo@vt.edu (D. Appelö), thagstrom@smu.edu (T. Hagstrom).

https://doi.org/10.1016/j.jcp.2025.114111
Received 25 September 2024; Received in revised form 31 March 2025; Accepted 19 May 2025
Available online 24 May 2025
0021-9991/© 2025 The Author(s). Published by Elsevier Inc. This is an open access article under the CC BY license (http://creativecommons.org/licenses/by/4.0/).

The difficulty in designing a systematic approach to handle the boundary conditions has prevented the use of the Hermite-Taylor method for many engineering and real-world scientific problems. Hybrid DG-Hermite methods were proposed to circumvent this issue by taking advantage of a DG method to handle the boundary conditions on complex geometries [15,16]. A DG solver is used on an unstructured or boundary fitted curvilinear mesh which encloses a Cartesian mesh where the Hermite method is applied. A local time-stepping procedure is needed to retain the large time-step sizes of the Hermite method.

Another method based on compatibility boundary conditions was developed for the wave equation on Cartesian and curvilinear meshes [17]. In d dimensions, this method computes the $(m+1)^d$ degrees of freedom on the boundary by enforcing the physical boundary condition as well as the compatibility boundary conditions. However, the extension of this method to first order hyperbolic systems is not straightforward due to the need for a characteristic decomposition and the presence of characteristic variables for the Maxwell system.

In [18], the Hermite-Taylor correction function method was proposed to handle general boundary conditions for Maxwell's equations. This method relies on the correction function method (CFM) to update the numerical solution and its derivatives where the Hermite-Taylor method cannot be applied. The correction function method seeks space-time polynomial approximations of the solution in small domains, called local patches, near the boundary or the interface by minimizing a functional. The functional is based on a square measure of the residual of the governing equations, boundary or interface conditions and the numerical solution from the original method (here the Hermite-Taylor method). The CFM minimization procedure provides polynomial approximations, also called correction functions, that are used to compute the $(m+1)^d$ degrees of freedom at the nodes where the Hermite-Taylor method cannot be applied. The CFM was first developed to enhance finite-difference methods for Poisson's equation with interface conditions [19,20]. It has been extended to the wave equation [21] and Maxwell's equations [7,22,23].

From a CFM point of view, the Hermite-Taylor setting provides several advantages compared to finite-difference methods. Indeed, the Hermite method uses a stencil that remains the same regardless of its order and naturally provides space-time polynomials approximating the solution that are required in the CFM functional. The Hermite-Taylor correction function method presented in [18] achieved up to a seventh-order rate of convergence with a loose CFL constant but was limited to boundaries aligned with the nodes. In this paper, we extend the Hermite-Taylor correction function method to embedded boundary and interface problems. We consider the situation where the mesh resolution allows the numerical solution from the original method to be available around the interface and boundary. In other words, interfaces and boundaries are sufficiently far away from each other to construct CFM local patches, leaving close contact interface problems for future work.

The paper is organized as follows. We introduce Maxwell's equations with boundary and interface conditions in Section 2. The Hermite-Taylor method in two space dimensions is presented in detail in Section 3. The correction function method in the Hermite-Taylor setting for embedded boundary and interface problems is described in Section 4. Finally, in Section 5, numerical examples in one and two space dimensions, including problems with discontinuous electromagnetic fields, are performed to verify the properties of the Hermite-Taylor correction function method.

2. Problem definition

In this work, we are seeking numerical solutions to Maxwell's equations

$$\begin{aligned} \mu(\boldsymbol{x})\,\partial_t \boldsymbol{H} + \nabla \times \boldsymbol{E} &= 0, \\ \epsilon(\boldsymbol{x})\,\partial_t \boldsymbol{E} - \nabla \times \boldsymbol{H} &= -\boldsymbol{J}, \\ \nabla \cdot (\epsilon(\boldsymbol{x})\,\boldsymbol{E}) &= \rho, \\ \nabla \cdot (\mu(\boldsymbol{x})\,\boldsymbol{H}) &= 0, \end{aligned} \tag{1}$$

in a domain $\Omega \subset \mathbb{R}^d$ $(d = 1, 2)$ and a time interval $I = [t_0, t_f]$. Here $\boldsymbol{H}$ is the magnetic field, $\boldsymbol{E}$ is the electric field, $\mu(\boldsymbol{x}) > 0$ is the magnetic permeability and $\epsilon(\boldsymbol{x}) > 0$ is the electric permittivity. The initial conditions are given by

$$\begin{aligned} \boldsymbol{H}(\boldsymbol{x}, 0) &= \boldsymbol{H}_0(\boldsymbol{x}) \quad \text{in } \Omega, \\ \boldsymbol{E}(\boldsymbol{x}, 0) &= \boldsymbol{E}_0(\boldsymbol{x}) \quad \text{in } \Omega, \end{aligned} \tag{2}$$

and the boundary condition is given by

$$\boldsymbol{n} \times \boldsymbol{E} = \boldsymbol{g}(\boldsymbol{x}, t) \quad \text{on } \partial\Omega \times I. \tag{3}$$

Here $\partial\Omega$ is the smooth boundary of the domain Ω, $\boldsymbol{n}$ is the outward unit normal to $\partial\Omega$ and $\boldsymbol{g}(\boldsymbol{x}, t)$ is a known function. Note that the situation where $\boldsymbol{g} = 0$ corresponds to perfect electric conductor (PEC) boundary conditions. For results on the well-posedness of Maxwell's equations with PEC boundary conditions, we refer the reader to [24].

We also consider Maxwell's interface problems. In this situation, the domain Ω is subdivided into two subdomains Ω^+ and Ω^-, and is such that $\Omega = \Omega^+ \cup \Omega^-$ and $\Omega^+ \cap \Omega^- = \Gamma$. Here Γ is the smooth interface between the subdomains. Fig. 1 illustrates a typical geometry of a domain Ω.

The physical parameters are assumed to be piecewise constant and are given by

$$\mu(\boldsymbol{x}) = \begin{cases} \mu^+ & \text{for} \quad \boldsymbol{x} \in \Omega^+, \\ \mu^- & \text{for} \quad \boldsymbol{x} \in \Omega^-, \end{cases} \tag{4}$$

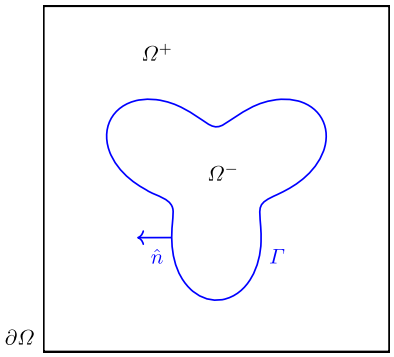

Fig. 1. Geometry of a domain Ω. The domain consists of two materials.

and

$$\epsilon(\boldsymbol{x}) = \begin{cases} \epsilon^+ & \text{for} \quad \boldsymbol{x} \in \Omega^+, \\ \epsilon^- & \text{for} \quad \boldsymbol{x} \in \Omega^-. \end{cases} \tag{5}$$

To complete Maxwell's equations, we impose the interface conditions

$$\begin{aligned} \hat{\boldsymbol{n}} \times [\![\boldsymbol{E}]\!] &= 0 \quad \text{on } \Gamma \times I, \\ \hat{\boldsymbol{n}} \times [\![\boldsymbol{H}]\!] &= 0 \quad \text{on } \Gamma \times I, \\ \hat{\boldsymbol{n}} \cdot [\![\epsilon\, \boldsymbol{E}]\!] &= 0 \quad \text{on } \Gamma \times I, \\ \hat{\boldsymbol{n}} \cdot [\![\mu\, \boldsymbol{H}]\!] &= 0 \quad \text{on } \Gamma \times I. \end{aligned} \tag{6}$$

Here $[\![\boldsymbol{H}]\!] = \boldsymbol{H}^+ - \boldsymbol{H}^-$ is the jump of the variable $\boldsymbol{H}$ on the interface, $\boldsymbol{H}^+$ is the solution in Ω^+, $\boldsymbol{H}^-$ is the solution in Ω^- and $\hat{\boldsymbol{n}}$ is the unit normal to the interface Γ.

In what follows we will assume for simplicity that $\boldsymbol{J} = 0$, $\rho = 0$. The construction of the boundary and interface conditions are unchanged so long as the currents are supported in the volume.

3. Hermite-Taylor method

In this section, for completeness, we briefly describe the Hermite-Taylor method, introduced by Goodrich et al. [14], to handle linear hyperbolic problems. For simplicity, the Hermite-Taylor method is presented in 2-D using the transverse magnetic (TM_z) mode. In this situation, Maxwell's equations are simplified to

$$\begin{aligned} \mu\, \partial_t H_x + \partial_y E_z &= 0, \\ \mu\, \partial_t H_y - \partial_x E_z &= 0, \\ \epsilon\, \partial_t E_z - \partial_x H_y + \partial_y H_x &= 0, \\ \partial_x H_x + \partial_y H_y &= 0, \end{aligned} \tag{7}$$

in a domain $\Omega = [x_\ell, x_r] \times [y_b, y_t]$ and a time interval $I = [t_0, t_f]$. Here we assume the physical parameters μ and ϵ to be constant. We consider initial conditions on H_x, H_y and E_z, and periodic boundary conditions.

The Hermite-Taylor method uses a mesh that is staggered in space and time. The primal mesh is defined as

$$(x_i, y_j) = (x_\ell + i\,\Delta x, y_b + j\,\Delta y), \quad i = 0, \dots, N_x, \quad j = 0, \dots, N_y, \tag{8}$$

with

$$\Delta x = \frac{x_r - x_\ell}{N_x}, \quad \Delta y = \frac{y_t - y_b}{N_y}. \tag{9}$$

Here N_x and N_y are respectively the number of cells in the x and y directions. The numerical solution on the primal mesh is centered at times

$$t_n = t_0 + n\,\Delta t, \quad n = 0, \dots, N_t, \quad \Delta t = \frac{t_f - t_0}{N_t}. \tag{10}$$

Here N_t is the required number of time steps to reach t_f. The nodes of the dual mesh are located at the cell centers of the primal mesh

$$(x_{i+1/2}, y_{j+1/2}) = (x_\ell + (i + 1/2)\,\Delta x, y_b + (j + 1/2)\,\Delta y), \tag{11}$$

for $i = 0, \dots, N_x - 1$, $j = 0, \dots, N_y - 1$, and at times

$$t_{n+1/2} = t_0 + (n + 1/2)\,\Delta t, \quad n = 0, \dots, N_t - 1. \tag{12}$$

The Hermite-Taylor method requires three processes to evolve the electromagnetic fields and their spatial derivatives through order m from the primal mesh at t_n to the dual mesh at $t_{n+1/2}$:

Hermite interpolation

Let us consider a sufficiently accurate approximation of each electromagnetic field component, for example E_z, and its derivatives $\frac{\partial^{k+\ell} E_z}{\partial x^k \partial y^\ell}$, $k, \ell = 0, \dots, m$, on the primal mesh at time t_n. For each cell $[x_i, x_{i+1}] \times [y_j, y_{j+1}]$ of the primal mesh and for each electromagnetic field component, we compute the unique degree $(2m+1)^2$ tensor-product polynomial satisfying the value and the given derivatives of the electromagnetic field components at the corners of the cell. The resulting polynomial is known as the Hermite interpolant.

Recursion relation

For each cell of the primal mesh and for each electromagnetic field, we identify the derivatives of the Hermite interpolant at the cell center as scaled coefficients, denoted by $c^{H_x}_{k,\ell}(t)|_{t_n}$, $c^{H_y}_{k,\ell}(t)|_{t_n}$ and $c^{E_z}_{k,\ell}(t)|_{t_n}$. Expanding each scaled coefficient of the Hermite interpolant in time using

$$c_{k,\ell}(t) = \sum_{s=0}^{q} c_{k,\ell,s} \left(\frac{t - t_n}{\Delta t} \right)^s \tag{13}$$

gives us a space-time polynomial, referred to as the Hermite-Taylor polynomial, approximating each electromagnetic field. We then enforce Maxwell's equations and its derivatives at the cell center to obtain a recursion relation for the scaled coefficients of the Hermite-Taylor polynomials

$$\begin{aligned} c^{H_x}_{k,\ell,s} &= -\frac{(\ell+1)\,\Delta t}{\mu\, s \Delta y} c^{E_z}_{k,\ell+1,s-1}, \\ c^{H_y}_{k,\ell,s} &= \frac{(k+1)\,\Delta t}{\mu\, s \Delta x} c^{E_z}_{k+1,\ell,s-1}, \\ c^{E_z}_{k,\ell,s} &= \frac{\Delta t}{\epsilon\, s} \left(\frac{(k+1)}{\Delta x} c^{H_y}_{k+1,\ell,s-1} - \frac{(\ell+1)}{\Delta y} c^{H_x}_{k,\ell+1,s-1} \right), \end{aligned} \tag{14}$$

for $k, \ell = 0, \dots, 2m+1$ and $s = 1, \dots, q$. Here $q = \nu(2m+1)$ in $\mathbb{R}^\nu$ so the Taylor expansion in time of the coefficients of Hermite interpolants is done exactly.

Time evolution

For each cell and for each electromagnetic field, we update the numerical solution on the dual mesh by evaluating the Hermite-Taylor polynomials at the cell center $(x_{i+1/2}, y_{j+1/2})$ and time $t_{n+1/2}$.

To complete the time step, we repeat a similar procedure for each cell $[x_{i-1/2}, x_{i+1/2}] \times [y_{j-1/2}, y_{j+1/2}]$ of the dual mesh at time $t_{n+1/2}$ and update the data on the primal mesh at (x_i, y_j) at t_{n+1}. The whole procedure is then repeated until the final time is reached.

In the situation where the derivatives cannot be easily computed, we project the initial solution onto a polynomial space of degree at least $2m+1$ to maintain accuracy. To do so, for each electromagnetic field and for each primal node (x_i, y_j), we define the spatial domain $[x_{i-1/2}, x_{i+1/2}] \times [y_{j-1/2}, y_{j+1/2}]$ and project the initial solution on the space of degree $(2m+2)^2$ tensor-product Legendre polynomials. We then approximate the required derivatives of each electromagnetic field at (x_i, y_j) using the derivatives of the Legendre polynomials approximating the electromagnetic fields.

The enforcement of boundary conditions is challenging for the Hermite-Taylor method since all values of the electromagnetic fields and their derivatives through order m in normal and tangential directions must also be known on the boundary, which is not the case in general. For an embedded boundary, the boundary can be located between the nodes of the mesh which further complicates the enforcement of boundary conditions. The imposition of interface conditions shares the same issue with the additional difficulty that the electromagnetic fields could be discontinuous at the interface. In the next section, we present a new avenue to handle embedded boundary and interface conditions based on the correction function method.

4. Correction function method

The correction function method seeks a polynomial approximating each electromagnetic field component in the vicinity of the nodes where the Hermite-Taylor method cannot be directly applied. We refer to such a node as a CF node. The node where the numerical solution can be updated using the Hermite-Taylor method is referred to as a Hermite node. The correction function method relies on the minimization of a functional describing the electromagnetic fields in the vicinity of a CF node. The approximations of the electromagnetic fields are sought in a polynomial space and a careful definition of the space-time domain of the polynomials approximating the electromagnetic fields is required for accuracy. In this section, we describe in detail the correction function method in 1-D for embedded boundary and interface problems. We then extend the method to the two-dimensional case.

4.1. Embedded boundary in one dimension

Let us consider the following 1-D simplification of Maxwell's equations

$$\begin{aligned} \mu\, \partial_t H + \partial_x E &= 0, \\ \epsilon\, \partial_t E + \partial_x H &= 0, \end{aligned} \tag{15}$$

in the domain $\Omega = [x_\ell, x_r]$ and the time interval $[t_0, t_f]$. Here μ and ϵ are constant. We enforce the boundary conditions

$$E(x_\ell, t) = g_\ell(t) \qquad \text{and} \qquad E(x_r, t) = g_r(t). \tag{16}$$

We consider the physical domain Ω to be embedded in a computational domain $\Omega_c = [x_0, x_N]$. We then have two CF nodes, one for the left boundary and one for the right boundary. For simplicity, we assume that both CF nodes belong to the primal mesh.

For the q^{th} CF node at time t_n, we define a functional

$$J_q^n = \mathcal{G}_q^n + \mathcal{B}_q^n + \mathcal{H}_q^n. \tag{17}$$

The first part $\mathcal{G}_q^n$ ensures that the governing equations are approximately fulfilled. The second part $\mathcal{B}_q^n$ weakly enforces the boundary conditions. The third part $\mathcal{H}_q^n$ weakly enforces the correction functions to match the Hermite solution. Note that the scaling of each part is determined by a dimensional analysis and is detailed in Remark 1.

Each part of the functional J_q^n is computed over different domains. The electromagnetic fields are required to approximately satisfy Maxwell's equations in the local patch of J_q^n. The space-time domain of the governing equations functional $\mathcal{G}_q^n$ then encloses the q^{th} CF node, the domains of the boundary functional $\mathcal{B}_q^n$ and the Hermite functional $\mathcal{H}_q^n$. The domain of $\mathcal{B}_q^n$ encloses the part of the boundary close to the q^{th} CF node. Finally, the domain of $\mathcal{H}_q^n$ encloses the space-time domains of the closest primal Hermite and dual Hermite nodes to the q^{th} CF node.

As an example, let us consider that the left boundary is located at x_ℓ between the dual node $x_{1/2}$ and the primal node x_1, so the zeroth CF node ($q = 0$) is associated with x_1. In this situation, we use the correction function method to update the numerical approximation to the electromagnetic fields and their m first derivatives located at the primal CF node x_1 at a given time t_n.

The governing equations functional $\mathcal{G}_0^n$ contains the residual of Maxwell's equations and is integrated over the space-time domain $S_0 \times [t_{n-1}, t_n]$. Here the space interval is $S_0 = [x_\ell, x_{5/2}]$. The governing equations functional is then given by

$$\mathcal{G}_0^n(H_{h,0}^n, E_{h,0}^n) = \frac{\ell_0}{2} \int_{t_{n-1}}^{t_n} \int_{S_0} (\mu\, \partial_t H_{h,0}^n + \partial_x E_{h,0}^n)^2 + Z^2(\epsilon\, \partial_t E_{h,0}^n + \partial_x H_{h,0}^n)^2 \,\mathrm{d}x\,\mathrm{d}t. \tag{18}$$

Here $Z = \sqrt{\mu/\epsilon}$ is the impedance and $\ell_0 = x_{5/2} - x_\ell$ is the characteristic length of the local patch, and $H_{h,0}^n$ and $E_{h,0}^n$ are the polynomials approximating the electromagnetic fields in the local patch that we seek. $H_{h,0}^n$ and $E_{h,0}^n$ are referred to as the correction functions. The integration domain of $\mathcal{G}_0^n$ is illustrated in Fig. 2.

The boundary functional $\mathcal{B}_0^n$ contains the residual of the boundary condition at x_ℓ and is integrated over the time interval $[t_{n-1}, t_n]$. We then have

$$\mathcal{B}_0^n(E_{h,0}^n) = \frac{1}{2} \int_{t_{n-1}}^{t_n} (E_{h,0}^n(x_\ell, t) - g_\ell(t))^2 \,\mathrm{d}t. \tag{19}$$

The integration domain of $\mathcal{B}_0^n$ is illustrated in Fig. 3.

Unfortunately, as shown in the numerical results of Section 5, the enforcement of only the boundary condition (3) leads either to an unstable method or a severe restriction on the CFL constant. Although the CFM, in general, impacts the stability of the original method, the numerical results reported in [7,23] for finite-difference methods and [18] for Hermite methods (limited to boundaries aligned with the mesh nodes) did not suffer from a significant CFL number reduction.

For embedded boundary and interface problems, the main difference between the method proposed here and previous works on finite-difference methods is that the original method is coupled to the CFM with not only the values of the correction functions but also their spatial derivatives through order m. This motivates us to add additional constraints on the spatial derivatives of the correction

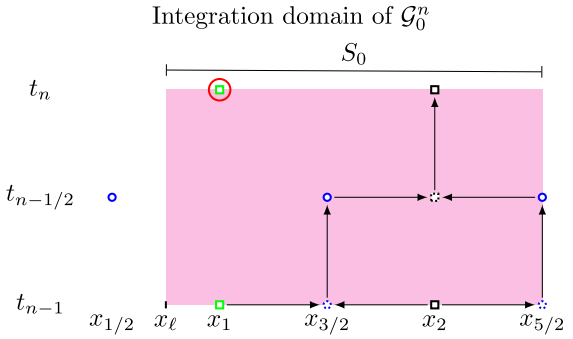

Fig. 2. Illustration of the domain of integration $S_0 \times [t_{n-1}, t_n]$ of $\mathcal{G}_0^n$. The primal CF and Hermite nodes are respectively represented by green squares and black squares while the dual Hermite nodes are represented by blue circles. The CFM seeks the information located at (x_1, t_n) which is enclosed by the red circle. The space-time local patch $S_0 \times [t_{n-1}, t_n]$ is denoted by a magenta box. (For interpretation of the references to colour in this figure legend, the reader is referred to the web version of this article.)

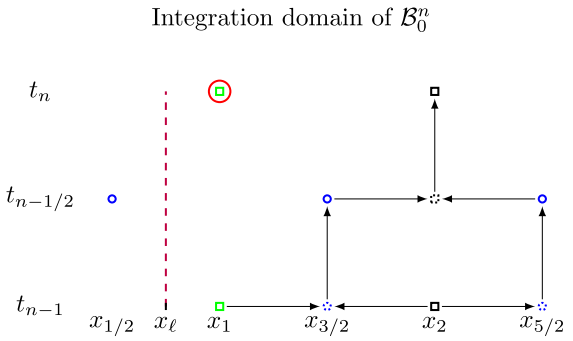

Fig. 3. Illustration of the domain of integration $[t_{n-1}, t_n]$ at x_ℓ of $\mathcal{B}_0^n$. The primal CF and Hermite nodes are respectively represented by green squares and black squares while the dual Hermite nodes are represented by blue circles. The CFM seeks the information located at (x_1, t_n) which is enclosed by the red circle. The intersection between the boundary and the local patch, that is the line connecting (x_ℓ, t_{n-1}) to (x_ℓ, t_n), is denoted by a dashed purple line. (For interpretation of the references to colour in this figure legend, the reader is referred to the web version of this article.)

functions at the boundary using compatibility conditions for improving the stability of the overall method. Compatibility conditions were used to enforce boundary and interface conditions in high-order finite-difference methods for Navier-Stokes equations [25], conservation laws [26], wave equation [27] and Maxwell's equations [4,6,28,29], to name a few. Recently, this approach was also used to enforce boundary conditions when dissipative and conservative Hermite methods are used for the scalar wave equation. For the CFM, we propose to use the time derivatives of boundary conditions and convert them into spatial derivatives, similar to what is done for inverse Lax-Wendroff methods [26] for conservation laws. Note that, in this situation, we do not use the compatibility conditions to obtain solvable linear systems that enforce the boundary (or interface) conditions (see Propositions 1 and 2), but rather to improve the stability of the proposed Hermite-Taylor correction function method.

Taking time derivatives of the left boundary condition lead to

$$\partial_t^j E(x_\ell, t) = \partial_t^j g_\ell(t). \tag{20}$$

Using now the 1-D simplification of Maxwell's Eq. (15) to convert the time derivatives of the electric field into spatial derivatives, we obtain

$$\partial_t^j E = \begin{cases} -\partial_x^j H/(\epsilon^\theta\, \mu^{\theta-1}), & \text{if } j \text{ odd}, \\ \partial_x^j E/(\epsilon\, \mu)^{j/2}, & \text{otherwise}. \end{cases} \tag{21}$$

Here $\theta = (j+1)/2$. Thus, the boundary functional becomes

$$\mathcal{B}_0^n(E_{h,0}^n) = \frac{1}{2}\sum_{j=0}^{N_d}\left(\frac{\ell_0}{c}\right)^{2j}\int_{t_{n-1}}^{t_n}(\partial_t^j E_{h,0}^n(x_\ell, t) - \partial_t^j g_\ell(t))^2\,\mathrm{d}t. \tag{22}$$

Here $c = 1/\sqrt{\epsilon\,\mu}$ is the wave speed, and N_d is the maximum order of the derivatives that are considered.

The Hermite functional

$$\mathcal{H}_0^n = \mathcal{H}_{p,0}^n + \mathcal{H}_{d,0}^n, \tag{23}$$

weakly enforces the correction function to match the Hermite solution. The first part $\mathcal{H}_{p,0}^n$ weakly enforces the correction function to match the Hermite-Taylor polynomial associated with the primal Hermite node x_2 in the space-time domain $S_{p,0}^{\mathcal{H}} \times [t_{n-1/2}, t_n]$. Here the space interval $S_{p,0}^{\mathcal{H}} = [x_{3/2}, x_{5/2}]$. We obtain

$$\mathcal{H}_{p,0}^n(H_{h,0}^n, E_{h,0}^n) = \frac{1}{2}\frac{c_H}{\Delta x}\int_{t_{n-\frac{1}{2}}}^{t_n}\int_{S_{p,0}^{\mathcal{H}}} Z^2(H_{h,0}^n - H^*)^2 + (E_{h,0}^n - E^*)^2\,\mathrm{d}x\,\mathrm{d}t. \tag{24}$$

Here $c_H > 0$ is a given penalization parameter, and H^* and E^* are Hermite-Taylor polynomials. The second term $\mathcal{H}_{d,0}^n$ weakly enforces the Hermite-Taylor polynomial associated with the dual Hermite node $x_{3/2}$ in the space-time domain $S_{d,0}^{\mathcal{H}} \times [t_{n-1}, t_{n-1/2}]$. Here the space interval is $S_{d,0}^{\mathcal{H}} = [x_1, x_2]$. We then have

$$\mathcal{H}_{d,0}^n(H_{h,0}^n, E_{h,0}^n) = \frac{1}{2}\frac{c_H}{\Delta x}\int_{t_{n-1}}^{t_{n-\frac{1}{2}}}\int_{S_{d,0}^{\mathcal{H}}} Z^2(H_{h,0}^n - H^*)^2 + (E_{h,0}^n - E^*)^2\,\mathrm{d}x\,\mathrm{d}t. \tag{25}$$

The integration domain of $\mathcal{H}_0^n$ is illustrated in Fig. 4. The procedure described above can be easily adapted to weakly enforce the boundary condition at x_r.

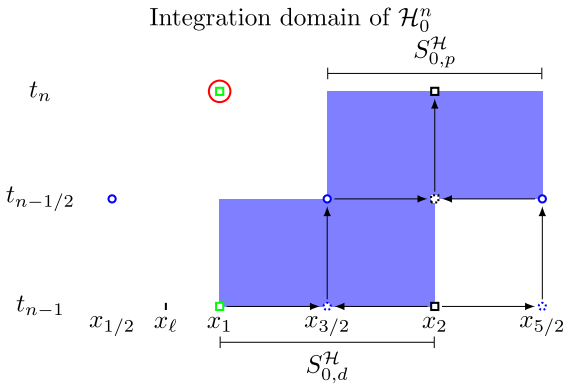

Fig. 4. Illustration of the domains of integration $S_{p,0}^{\mathcal{H}} \times [t_{n-1/2}, t_n]$ and $S_{d,0}^{\mathcal{H}} \times [t_{n-1}, t_{n-1/2}]$ of $\mathcal{H}_0^n$. The primal CF and Hermite nodes are respectively represented by green squares and black squares while the dual Hermite nodes are represented by blue circles. The CFM seeks the information located at (x_1, t_n) which is enclosed by the red circle. The domains $S_{p,0}^{\mathcal{H}} \times [t_{n-1/2}, t_n]$ and $S_{d,0}^{\mathcal{H}} \times [t_{n-1}, t_{n-1/2}]$, where we enforce the correction functions to match the Hermite-Taylor polynomials, are denoted by blue boxes. (For interpretation of the references to colour in this figure legend, the reader is referred to the web version of this article.)

Remark 1. The choice of the scaling of the different parts of the functional J_q^n is dictated by a dimensional analysis. In other words, the different terms share all the same dimensional unit. Consider

$$\boldsymbol{x} = L_0 \hat{\boldsymbol{x}}, \quad t = \frac{L_0}{c_0}\hat{t}, \quad \boldsymbol{E} = H_0 Z_0 \hat{\boldsymbol{E}}, \quad \boldsymbol{H} = H_0 \hat{\boldsymbol{H}}, \quad \mu^{\pm} = \mu_0 \hat{\mu}^{\pm}, \quad \epsilon^{\pm} = \epsilon_0 \hat{\epsilon}^{\pm}, \tag{26}$$

where $\hat{\boldsymbol{x}}$ represents a non-dimensional variable associated with $\boldsymbol{x}$, L_0 is the reference length, H_0 is the reference magnetic strength, $c_0 = 1/\sqrt{\epsilon_0 \mu_0}$ is the dimensional speed of light in free space, and $Z_0 = \sqrt{\mu_0/\epsilon_0}$. Substituting these in the different terms of the functional J_q^n shows that they share the same dimensional unit, that is $Z_0^2 H_0^2 L_0^d / c_0$ in d space dimensions.

4.1.1. The linear system of equations that solves the optimization problem

For each CF node, we solve the following minimization problem

$$\begin{aligned} &\text{Find } (H_{h,q}^n, E_{h,q}^n) \in V \times V \text{ such that} \\ &(H_{h,q}^n, E_{h,q}^n) = \underset{v,w \in V}{\arg\min}\, J_q^n(v, w). \end{aligned} \tag{27}$$

Here $V = \mathbb{Q}^k\big(S_q \times [t_{n-1}, t_n]\big)$ is the space of tensor-product polynomials of degree at most k in each variable, $n = 1, \ldots, N_t$ and $q = 0, 1$ in our 1-D example. We use space-time Legendre polynomials as basis functions of V. To solve the minimization problem (27), we compute the gradient of J_q^n with respect to the coefficients of the polynomials $H_{h,q}^n$ and $E_{h,q}^n$ and use that it vanishes at a minimum. We then obtain the linear system of equations

$$M_q^n \boldsymbol{c}_q^n = \boldsymbol{b}_q^n. \tag{28}$$

Here M_q^n is a square matrix of dimension $2(k+1)^2$ and $\boldsymbol{c}_q^n$ is a vector containing the polynomials coefficients. Note that the dimension of the matrices M_q^n is independent of the mesh size.

Since the boundary is invariant in time, we have $M_q = M_q^n$ for all n and therefore obtain one matrix per CF node. The matrices, M_q, their scaling and their LU factorization are all precomputed. Note that the matrices M_q are scaled using row and column scalings. The scaling matrices are computed using only the block diagonal of M_q, where the diagonal blocks are $(k+1)^{d+1} \times (k+1)^{d+1}$ matrices in d space dimensions. For each time step, we then have to compute the right-hand side $\boldsymbol{b}_q^n$, perform forward and backward substitutions to find $\boldsymbol{c}_q^n$, and update the numerical solution of the electromagnetic fields and their first m derivatives at the q^{th} CF node using $H_{h,q}^n$ and $E_{h,q}^n$. This can be done independently for each q.

Remark 2. A similar procedure can be done to update the data located at dual CF nodes. However, the electromagnetic fields and their first m space derivatives at time $t_{-1/2}$ are required. In this work, we consider that these data are provided. Note that it would also be possible to use Hermite-Taylor polynomials obtained with the initial data at t_0 to estimate the required data at $t_{-1/2}$.

Assume that there are CF nodes on the primal and dual meshes. Given the numerical solution on the primal mesh at t_{n-1} and on the dual mesh at $t_{n-3/2}$, the algorithm to evolve the numerical solution at t_n is

1. Update the numerical solution on the dual Hermite node at $t_{n-1/2}$ using the Hermite-Taylor method and store the Hermite-Taylor polynomials needed for the CFM;
2. Update the numerical solution on the dual CF nodes at $t_{n-1/2}$ using the CFM by computing $\boldsymbol{b}_q^{n-1/2}$ and solving for $\boldsymbol{c}_q^{n-1/2}$;
3. Update the numerical solution on the primal Hermite node at t_n using the Hermite-Taylor method and store the Hermite-Taylor polynomials needed for the CFM;
4. Update the numerical solution on the primal CF nodes at t_n using the CFM by computing $\boldsymbol{b}_q^n$ and solving for $\boldsymbol{c}_q^n$.

4.2. Interface in one dimension

Let us now consider 1-D interface problems. In addition to Maxwell's Eq. (15), we consider the interface conditions

$$[\![H]\!] = 0 \qquad \text{and} \qquad [\![E]\!] = 0, \tag{29}$$

on the interface Γ located at x_Γ. We define the subdomains $\Omega^+ = [x_\ell, x_\Gamma]$ and $\Omega^- = [x_\Gamma, x_r]$. The physical parameters μ and ϵ are assumed to be piecewise constant. In this situation, we seek approximations of the electromagnetic fields in each subdomain for a given CF node. For each CF node, we then compute $H_h^{+,n}$ and $E_h^{+,n}$ approximating the electromagnetic fields in Ω^+, and $H_h^{-,n}$ and $E_h^{-,n}$ approximating the electromagnetic fields in Ω^-.

For the q^{th} CF node at time t_n, we define a functional

$$J_q^n = \mathcal{G}_q^{+,n} + \mathcal{G}_q^{-,n} + \mathcal{I}_q^n + \mathcal{H}_q^{+,n} + \mathcal{H}_q^{-,n}. \tag{30}$$

The governing equations functionals $\mathcal{G}_q^{+,n}$ and $\mathcal{G}_q^{-,n}$ ensure that Maxwell's equations in respectively Ω^+ and Ω^- are approximately fulfilled. The interface functional $\mathcal{I}_q^n$ weakly enforces the interface conditions. The Hermite functional $\mathcal{H}_q^{+,n}$ weakly enforces the correction functions $H_{h,q}^{+,n}$ and $E_{h,q}^{+,n}$ to match the Hermite solution in Ω^+ while $\mathcal{H}_q^{-,n}$ weakly enforces the correction functions $H_{h,q}^{-,n}$ and $E_{h,q}^{-,n}$ to match the Hermite solution in Ω^-.

As for embedded boundary problems, each part of the functional J_q^n is computed in different domains. The domains of $\mathcal{G}_q^{+,n}$ and $\mathcal{G}_q^{-,n}$ enclose the q^{th} CF node, the domains of the interface functional and the Hermite functionals. This then defines the local patch of the q^{th} CF node. The interface functional $\mathcal{I}_q^n$ encloses the part of the interface close to the q^{th} CF node. The Hermite functional $\mathcal{H}_q^{+,n}$ encloses the space-time domains of the closest primal Hermite and dual Hermite nodes in Ω^+ to the q^{th} CF node. Finally, the Hermite functional $\mathcal{H}_q^{-,n}$ encloses the domains of the closest primal Hermite and dual Hermite nodes in Ω^- to the q^{th} CF node.

As an example, we assume an interface Γ located at x_Γ between the dual node $x_{i+1/2}$ and the primal node x_{i+1}. In this situation, there are two CF nodes, one primal CF node located at x_{i+1} and one dual CF node located at $x_{i+1/2}$. We now focus on the primal CF node which we assume corresponds to the zeroth CF node ($q = 0$).

The governing equations functional $\mathcal{G}_0^{+,n}$ contains the residual of Maxwell's equations with the parameters from Ω^+ and is integrated over the domain $S_0 \times [t_{n-1}, t_n]$. Here the space interval $S_0 = [x_{i-1}, x_{i+5/2}]$. We have

$$\mathcal{G}_0^{+,n}(H_{h,0}^{+,n}, E_{h,0}^{+,n}) = \frac{\ell_0}{2} \int_{t_{n-1}}^{t_n} \int_{S_0} (\mu^+ \partial_t H_{h,0}^{+,n} + \partial_x E_{h,0}^{+,n})^2 + (Z^+)^2 (\epsilon^+ \partial_t E_{h,0}^{+,n} + \partial_x H_{h,0}^{+,n})^2 \, \mathrm{d}x \, \mathrm{d}t. \tag{31}$$

Here the characteristic length of the local patch is $\ell_0 = x_{i+5/2} - x_{i-1}$. The governing equations functional $\mathcal{G}_0^{-,n}$ is defined on the same domain as the functional $\mathcal{G}_0^{+,n}$ but contains the residual of Maxwell's equations with the parameters from Ω^-. We then have

$$\mathcal{G}_0^{-,n}(H_{h,0}^{-,n}, E_{h,0}^{-,n}) = \frac{\ell_0}{2} \int_{t_{n-1}}^{t_n} \int_{S_0} (\mu^- \partial_t H_{h,0}^{-,n} + \partial_x E_{h,0}^{-,n})^2 + (Z^-)^2 (\epsilon^- \partial_t E_{h,0}^{-,n} + \partial_x H_{h,0}^{-,n})^2 \, \mathrm{d}x \, \mathrm{d}t. \tag{32}$$

The domain of integration of the governing equations functionals $\mathcal{G}_0^{+,n}$ and $\mathcal{G}_0^{-,n}$ is shown in Fig. 5.

The interface functional $\mathcal{I}_0^n$ contains the residual of the interface conditions, which in this case we take to be continuity for E and H, and is integrated over the time interval $[t_{n-1}, t_n]$. We then have

$$\mathcal{I}_0^n(H_{h,0}^{+,n}, E_{h,0}^{+,n}, H_{h,0}^{-,n}, E_{h,0}^{-,n}) = \frac{1}{2} \sum_{j=0}^{N_d} \left(\frac{\ell_0}{c}\right)^{2j} \int_{t_{n-1}}^{t_n} \bar{Z}^2 \left[\!\left[\partial_t^j H_{h,0}^n(x_\Gamma, t)\right]\!\right]^2 + \left[\!\left[\partial_t^j E_{h,0}^n(x_\Gamma, t)\right]\!\right]^2 \mathrm{d}t. \tag{33}$$

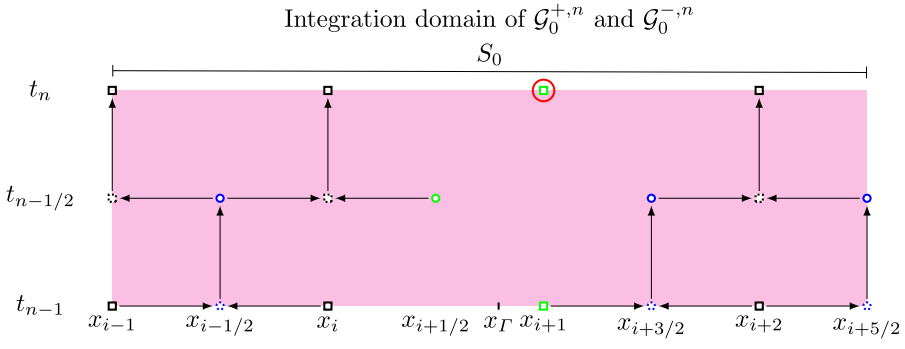

Fig. 5. Illustration of the domain of integration $S_0 \times [t_{n-1}, t_n]$ of $\mathcal{G}_0^{+,n}$ and $\mathcal{G}_0^{-,n}$. The primal CF and Hermite nodes are respectively represented by green squares and black squares while the dual CF and Hermite nodes are represented by green circles and blue circles. The CFM seeks the information located at (x_{i+1}, t_n) which is enclosed by the red circle. The space-time local patch $S_0 \times [t_{n-1}, t_n]$ is denoted by a magenta box. (For interpretation of the references to colour in this figure legend, the reader is referred to the web version of this article.)

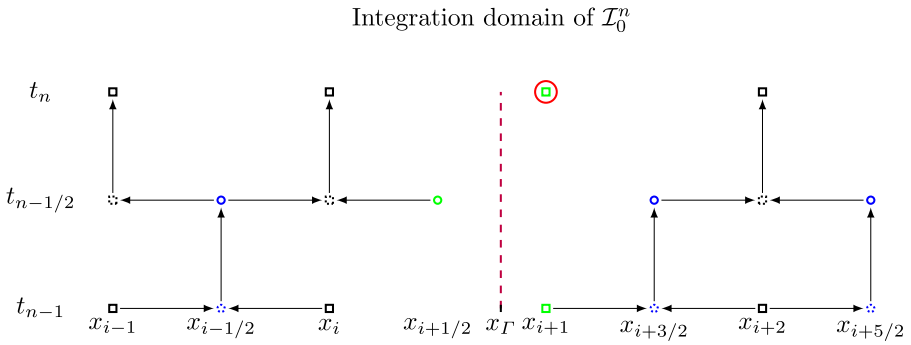

Fig. 6. Illustration of the domain of integration $[t_{n-1}, t_n]$ at x_Γ of $\mathcal{I}_0^n$. The primal CF and Hermite nodes are respectively represented by green squares and black squares while the dual CF and Hermite nodes are represented by green circles and blue circles. The CFM seeks the information located at (x_{i+1}, t_n) which is enclosed by the red circle. The intersection between the interface and the local patch, that is the line connecting (x_Γ, t_{n-1}) to (x_Γ, t_n), is denoted by a dashed purple line. (For interpretation of the references to colour in this figure legend, the reader is referred to the web version of this article.)

Here

$$\partial_t^j H = \begin{cases} -\partial_x^j E/(\epsilon^{\theta-1}\,\mu^\theta), & \text{if } j \text{ odd}, \\ \partial_x^j H/(\epsilon\,\mu)^{j/2}, & \text{otherwise}. \end{cases} \tag{34}$$

Note that the interface functional couples the electromagnetic fields from the different subdomains at the interface and that we convert the time derivatives of the electromagnetic fields into spatial derivatives using (21) and (34) to improve the stability of the Hermite-Taylor correction function method, as shown in the numerical results of Section 5. We can take $\bar{Z} = (Z^+ + Z^-)/2$ or the values from the left or right as convenient. The integration domain of $\mathcal{I}_0^n$ is illustrated in Fig. 6.

The Hermite functional $\mathcal{H}_0^{+,n}$ weakly enforces the correction functions $H_{h,0}^{+,n}$ and $E_{h,0}^{+,n}$ to match the Hermite solution in Ω^+ over the domains $S_{p,0}^{\mathcal{H}^+} \times [t_{n-1/2}, t_n]$ and $S_{d,0}^{\mathcal{H}^+} \times [t_{n-1}, t_{n-1/2}]$. Here $S_{p,0}^{\mathcal{H}^+} = [x_{i+3/2}, x_{i+5/2}]$ is the space interval of the primal Hermite node x_{i+2} and $S_{d,0}^{\mathcal{H}^+} = [x_{i+1}, x_{i+2}]$ is the space interval of the dual Hermite node $x_{i+3/2}$. We then have

$$\mathcal{H}_0^{+,n} = \mathcal{H}_{p,0}^{+,n} + \mathcal{H}_{d,0}^{+,n}, \tag{35}$$

with

$$\begin{aligned} \mathcal{H}_{p,0}^{+,n}(H_{h,0}^{+,n}, E_{h,0}^{+,n}) &= \frac{1}{2}\frac{c_H}{\Delta x} \int_{t_{n-\frac{1}{2}}}^{t_n} \int_{S_{p,0}^{\mathcal{H}^+}} (Z^+)^2 (H_{h,0}^{+,n} - H^*)^2 + (E_{h,0}^{+,n} - E^*)^2 \,\mathrm{d}x\,\mathrm{d}t, \\ \mathcal{H}_{d,0}^{+,n}(H_{h,0}^{+,n}, E_{h,0}^{+,n}) &= \frac{1}{2}\frac{c_H}{\Delta x} \int_{t_{n-1}}^{t_{n-\frac{1}{2}}} \int_{S_{d,0}^{\mathcal{H}^+}} (Z^+)^2 (H_{h,0}^{+,n} - H^*)^2 + (E_{h,0}^{+,n} - E^*)^2 \,\mathrm{d}x\,\mathrm{d}t. \end{aligned} \tag{36}$$

Finally, the Hermite functional $\mathcal{H}_0^{-,n}$ weakly enforces the correction functions $H_{h,0}^{-,n}$ and $E_{h,0}^{-,n}$ to match the Hermite solution in Ω^- over the domains $S_{p,0}^{\mathcal{H}^-} \times [t_{n-1/2}, t_n]$ and $S_{d,0}^{\mathcal{H}^-} \times [t_{n-1}, t_{n-1/2}]$. Here the space intervals $S_{p,0}^{\mathcal{H}^-} = [x_{i-1/2}, x_{i+1/2}]$ and $S_{d,0}^{\mathcal{H}^-} = [x_{i-1}, x_i]$. We obtain

$$\mathcal{H}_0^{-,n} = \mathcal{H}_{p,0}^{-,n} + \mathcal{H}_{d,0}^{-,n}, \tag{37}$$

with

$$\begin{aligned} \mathcal{H}_{p,0}^{-,n}(H_{h,0}^{-,n}, E_{h,0}^{-,n}) &= \frac{1}{2}\frac{c_H}{\Delta x} \int_{t_{n-\frac{1}{2}}}^{t_n} \int_{S_{p,0}^{\mathcal{H}^-}} (Z^-)^2 (H_{h,0}^{-,n} - H^*)^2 + (E_{h,0}^{-,n} - E^*)^2 \,\mathrm{d}x\,\mathrm{d}t, \\ \mathcal{H}_{d,0}^{-,n}(H_{h,0}^{-,n}, E_{h,0}^{-,n}) &= \frac{1}{2}\frac{c_H}{\Delta x} \int_{t_{n-1}}^{t_{n-\frac{1}{2}}} \int_{S_{d,0}^{\mathcal{H}^-}} (Z^-)^2 (H_{h,0}^{-,n} - H^*)^2 + (E_{h,0}^{-,n} - E^*)^2 \,\mathrm{d}x\,\mathrm{d}t. \end{aligned} \tag{38}$$

The integration domains of $\mathcal{H}_0^{+,n}$ and $\mathcal{H}_0^{-,n}$ are illustrated in Fig. 7.

A similar procedure is used to define the functional $J^{n-1/2}$ associated with the dual CF node $x_{i+1/2}$.

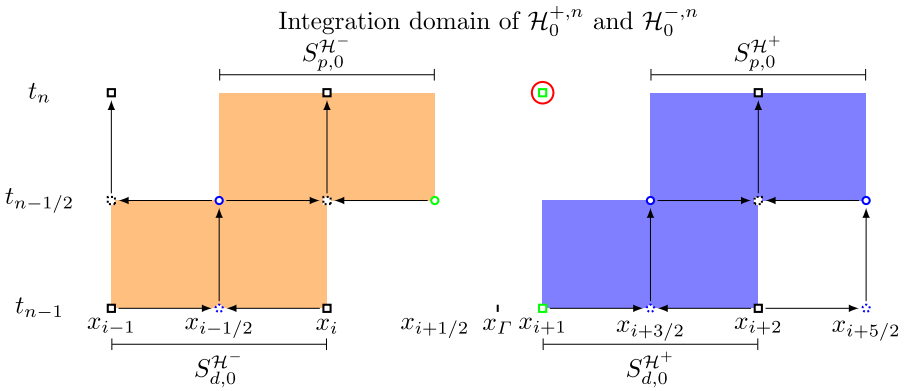

Fig. 7. Illustration of the domains of integration $S_{p,0}^{\mathcal{H}^+} \times [t_{n-1/2}, t_n]$, $S_{d,0}^{\mathcal{H}^+} \times [t_{n-1}, t_{n-1/2}]$, $S_{p,0}^{\mathcal{H}^-} \times [t_{n-1/2}, t_n]$ and $S_{d,0}^{\mathcal{H}^-} \times [t_{n-1}, t_{n-1/2}]$ of $\mathcal{H}_0^{+,n}$ and $\mathcal{H}_0^{-,n}$. The primal CF and Hermite nodes are respectively represented by green squares and black squares while the dual CF and Hermite nodes are represented by green circles and blue circles. The CFM seeks the information located at (x_{i+1}, t_n) which is enclosed by the red circle. The domains of $\mathcal{H}_0^{+,n}$ and $\mathcal{H}_0^{-,n}$, where we enforce the correction functions to match the Hermite-Taylor polynomials, are denoted respectively by blue boxes and orange boxes. (For interpretation of the references to colour in this figure legend, the reader is referred to the web version of this article.)

4.2.1. *The linear system of equations that solves the optimization problem*

For each CF node, we solve the following minimization problem

$$\begin{aligned} &\text{Find } (H_{h,q}^{+,n}, E_{h,q}^{+,n}, H_{h,q}^{-,n}, E_{h,q}^{-,n}) \in V \times V \times V \times V \text{ such that} \\ &(H_{h,q}^{+,n}, E_{h,q}^{+,n}, H_{h,q}^{-,n}, E_{h,q}^{-,n}) = \underset{v^+,w^+,v^-,w^- \in V}{\arg\min} \; J_q^n(v^+, w^+, v^-, w^-). \end{aligned} \tag{39}$$

We solve the minimization problem (39) using a procedure similar to that of the embedded boundary case. We therefore have the same properties as before, except that the dimension of the resulting linear system becomes $4(k+1)^2$. The algorithm of the Hermite-Taylor correction function method to evolve the numerical solution remains the same as for the embedded boundary case.

4.3. *Multi-dimensional case*

In this subsection, we extend the Hermite-Taylor correction function method to two and three dimensions for embedded boundary and interface problems.

4.3.1. *Computation of the local patches*

In the multi-dimensional case, the time component of the local patches remains the same for all CF nodes while their spatial components are adapted to the geometry of the boundary (or interface). The spatial component S_q of the local patch associated with the i^{th} CF node needs to satisfy the following three constraints:

1. The i^{th} CF node must be inside S_q;
2. The part of the boundary (or interface) closest to the i^{th} CF node must be included in S_q;
3. The cells of the Hermite nodes closest to the i^{th} CF node must be included in S_q.

To reduce the number of minimization problems, we base the construction of the local patches on a parametrization of the boundary or interface and associate multiple CF nodes to a local patch. In the following, the subscript q is now associated with the q^{th} local patch that contains multiple CF nodes.

Focusing in detail on two space dimensions for simplicity, we define the dimension of the spatial component S_q to be $\beta h \times \beta h$. Here $h = \Delta x = \Delta y$ is the mesh size and β is a given positive constant that depends on the geometry of the boundary (or interface). Since the update of the numerical solution with the Hermite-Taylor method for one half time step uses a five-node stencil, we therefore have one layer of CF nodes inside the domain along the boundary. As for the interface case, we have one layer of CF nodes inside each subdomain along the interface.

To construct the local patches, consider Γ to be a parametrized curve with respect to the parameter $s \in [s_a, s_b]$. We want to find the nodes s_q, discretizing Γ. The arc length ΔL_Γ between two nodes s_q and s_{q+1} on Γ is

$$\Delta L_\Gamma = \int_{s_q}^{s_{q+1}} \sqrt{\left(\frac{dx}{ds}\right)^2 + \left(\frac{dy}{ds}\right)^2}\, ds. \tag{40}$$

Starting at $s_0 = s_a$, requiring $\Delta L_\Gamma = \alpha h$ and approximating the integral with the trapezoidal rule, the remaining nodes s_q are approximated recursively using the secant method. Here α is a positive constant.

In the vicinity of each node s_q a local patch, S_q, is constructed. We first find the closest primal CF node to $(x(s_q), y(s_q))$ and center S_q at the spatial coordinate of this primal CF node, denoted as $\boldsymbol{x}_{s_q}$. The spatial component of the resulting local patch then encloses the closest part of the boundary (or interface) to the primal CF node located at $\boldsymbol{x}_{s_q}$ as well as its closest Hermite cells. For each of the remaining primal and dual CF nodes, we find q such that the distance to $\boldsymbol{x}_{s_q}$ is minimized and associate the corresponding local patch S_q to it. For a reasonable value of α, the requirements of the spatial component of the local patch should be satisfied for all CF nodes within a local patch. Once the space-time domains of the local patches are computed, it is easy to identify the primal and dual Hermite nodes located inside the local patches and compute the space-time regions for the Hermite functionals. There are two functionals $\mathcal{J}$ associated with a space-time local patch, one for the primal CF nodes and one for the dual CF nodes. Note that the difference is due to the time integration of the Hermite functionals $\mathcal{H}_p$ and $\mathcal{H}_d$. Figs. 8 and 9 illustrate examples of a local patch with $\beta = 5$ for respectively an embedded boundary problem and an interface problem.

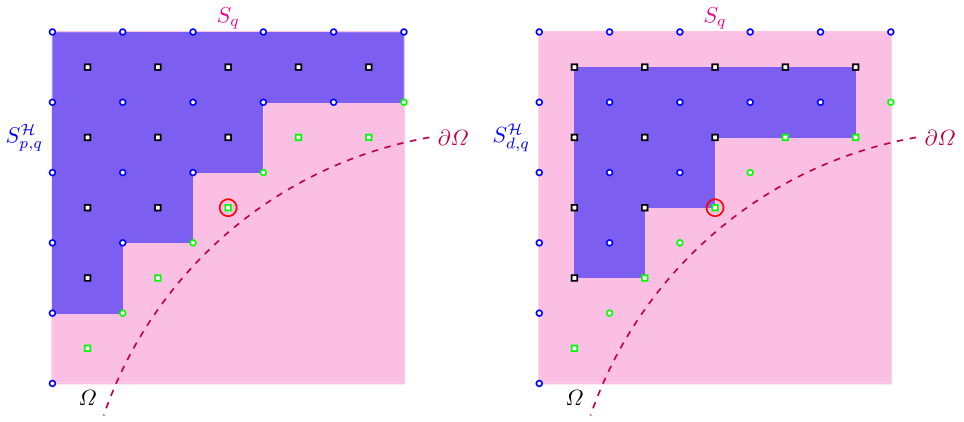

Fig. 8. Illustration of a 2-D local patch for an embedded boundary problem. The local patch is associated with the node s_q enclosed by the black circle and centered at the primal CF node enclosed by the dashed red diamond. The primal CF and Hermite nodes are respectively represented by green squares and black squares while the dual CF and Hermite nodes are represented by green circles and blue circles. The CFM seeks the information located at the CF nodes enclosed by a red diamond or circle. The spatial domain S_q of the local patch is denoted by a magenta box. The boundary $\partial\Omega$ is denoted by a dashed purple line. The domains $S^{\mathcal{H}}_{p,q}$ and $S^{\mathcal{H}}_{d,q}$ where we enforce the correction functions to match the Hermite-Taylor polynomials are denoted by blue boxes. The left plot is for the spatial components of the local patch over the time interval $[t_{n-1/2}, t_n]$ while the right plot is for $[t_{n-1}, t_{n-1/2}]$ when we update primal CF nodes at t_n. For the update of dual CF nodes at $t_{n+1/2}$, the time intervals for the left and right plots are respectively $[t_{n-1/2}, t_n]$ and $[t_n, t_{n+1/2}]$. (For interpretation of the references to colour in this figure legend, the reader is referred to the web version of this article.)

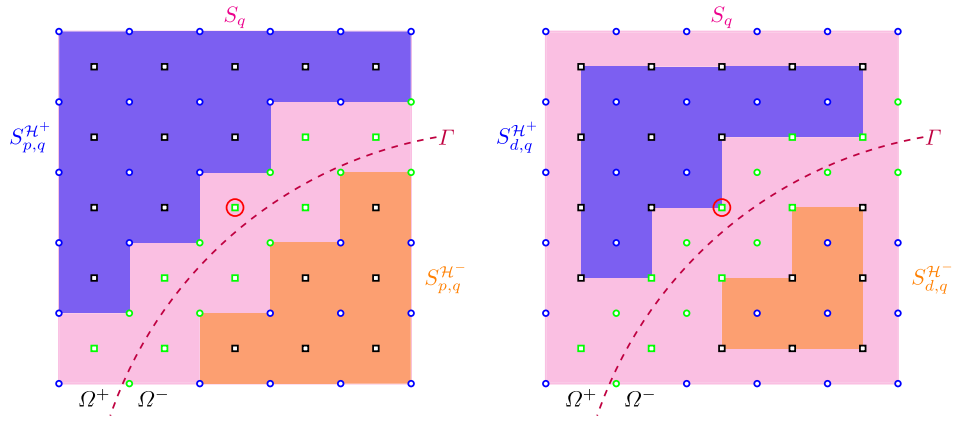

Fig. 9. Illustration of a 2-D local patch for an interface problem. The local patch is associated with the node s_q enclosed by the black circle and centered at the primal CF node enclosed by the dashed red diamond. The primal CF and Hermite nodes are respectively represented by green squares and black squares while the dual CF and Hermite nodes are represented by green circles and blue circles. The CFM seeks the information located at the CF nodes enclosed by a red diamond or circle. The spatial domain S_q of the local patch is denoted by a magenta box. The interface Γ is denoted by a dashed purple line. The domains $S^{\mathcal{H}^+}_{p,q}$ and $S^{\mathcal{H}^+}_{d,q}$ where we enforce the correction functions to match the Hermite-Taylor polynomials in Ω^+ are denoted by blue boxes. The domains $S^{\mathcal{H}^-}_{p,q}$ and $S^{\mathcal{H}^-}_{d,q}$ are denoted by orange boxes. The left plot is for the spatial components of the local patch over the time interval $[t_{n-1/2}, t_n]$ while the right plot is for $[t_{n-1}, t_{n-1/2}]$ when we update primal CF nodes at t_n. For the update of dual CF nodes at $t_{n+1/2}$, the time intervals for the left and right plots are respectively $[t_{n-1/2}, t_n]$ and $[t_n, t_{n+1/2}]$. (For interpretation of the references to colour in this figure legend, the reader is referred to the web version of this article.)

4.3.2. Definition of the correction function functional

Let us first focus on the embedded boundary case. For simplicity, we consider that all the CF nodes belong to the primal mesh. The described procedure below can be easily adapted to define the functional for a dual CF node. For each local patch, we define the functional (17) to seek the polynomials $\boldsymbol{H}^n_{h,q}$ and $\boldsymbol{E}^n_{h,q}$ approximating the electromagnetic fields in the local patch. The governing equations functional becomes

$$\begin{aligned}\mathcal{G}^n_q(\boldsymbol{H}^n_{h,q},\boldsymbol{E}^n_{h,q}) = \frac{\ell_q}{2}\int_{t_{n-1}}^{t_n}\int_{S_q}(\mu\,\partial_t\boldsymbol{H}^n_{h,q}+\nabla\times\boldsymbol{E}^n_{h,q})\cdot(\mu\,\partial_t\boldsymbol{H}^n_{h,q}+\nabla\times\boldsymbol{E}^n_{h,q})\\ +\ Z^2(\epsilon\,\partial_t\boldsymbol{E}^n_{h,q}-\nabla\times\boldsymbol{H}^n_{h,q})\cdot(\epsilon\,\partial_t\boldsymbol{E}^n_{h,q}-\nabla\times\boldsymbol{H}^n_{h,q})+c^2(\nabla\cdot(\mu\,\boldsymbol{H}^n_{h,q}))^2+\frac{1}{\epsilon^2}(\nabla\cdot(\epsilon\,\boldsymbol{E}^n_{h,q}))^2\,\mathrm{d}\boldsymbol{x}\,\mathrm{d}t.\end{aligned} \tag{41}$$

Here $\ell_q = \beta\,h$ is the characteristic length of the local patch. The second part of the functional J^n_q that weakly enforces the boundary condition (3) becomes

$$\mathcal{B}^n_q(\boldsymbol{E}^n_{h,q}) = \frac{1}{2}\sum_{j=0}^{N_d}\left(\frac{\ell_q}{c}\right)^{2s}\int_{t_{n-1}}^{t_n}\int_{\partial\Omega\cap S_q}(\boldsymbol{n}\times\partial_t^j\boldsymbol{E}^n_{h,q}-\partial_t^j\boldsymbol{g})\cdot(\boldsymbol{n}\times\partial_t^j\boldsymbol{E}^n_{h,q}-\partial_t^j\boldsymbol{g})\,\mathrm{d}s\,\mathrm{d}t. \tag{42}$$

Here

$$\partial_t^j\boldsymbol{E} = \begin{cases}\nabla^{j-1}(\nabla\times\boldsymbol{H})/(\epsilon^\theta\,\mu^{\theta-1}), & \text{if } j \text{ odd},\\ -\nabla^{j-2}(\nabla\times\nabla\times\boldsymbol{E})/(\epsilon\,\mu)^{j/2}, & \text{otherwise},\end{cases} \tag{43}$$

and $\theta = (j+1)/2$. Finally, the two parts in the Hermite functional $\mathcal{H}^n_q$ become

$$\begin{aligned}\mathcal{H}^n_{p,q}(\boldsymbol{H}^n_{h,q},\boldsymbol{E}^n_{h,q}) &= \frac{1}{2}\frac{c_H}{h}\int_{t_{n-\frac{1}{2}}}^{t_n}\int_{S^{\mathcal{H}}_{p,q}} Z^2(\boldsymbol{H}^n_{h,q}-\boldsymbol{H}^*)\cdot(\boldsymbol{H}^n_{h,q}-\boldsymbol{H}^*)+(\boldsymbol{E}^n_{h,q}-\boldsymbol{E}^*)\cdot(\boldsymbol{E}^n_{h,q}-\boldsymbol{E}^*)\,\mathrm{d}\boldsymbol{x}\,\mathrm{d}t,\\ \mathcal{H}^n_{d,q}(\boldsymbol{H}^n_{h,q},\boldsymbol{E}^n_{h,q}) &= \frac{1}{2}\frac{c_H}{h}\int_{t_{n-1}}^{t_{n-\frac{1}{2}}}\int_{S^{\mathcal{H}}_{d,q}} Z^2(\boldsymbol{H}^n_{h,q}-\boldsymbol{H}^*)\cdot(\boldsymbol{H}^n_{h,q}-\boldsymbol{H}^*)+(\boldsymbol{E}^n_{h,q}-\boldsymbol{E}^*)\cdot(\boldsymbol{E}^n_{h,q}-\boldsymbol{E}^*)\,\mathrm{d}\boldsymbol{x}\,\mathrm{d}t.\end{aligned} \tag{44}$$

As for the interface case, the functionals of the governing equations and the Hermite functionals in (30) are modified in the same way as the embedded boundary case. The interface functional that weakly enforces the interface conditions (6) becomes

$$\begin{aligned}\mathcal{I}^n_q(\boldsymbol{H}^{+,n}_{h,q},\boldsymbol{E}^{+,n}_{h,q},\boldsymbol{H}^{-,n}_{h,q},\boldsymbol{E}^{-,n}_{h,q}) = \frac{1}{2}\sum_{j=0}^{N_d}\left(\frac{\ell_q}{\bar{c}}\right)^{2j}\int_{t_{n-1}}^{t_n}\int_{\Gamma\cap S_q}\left(\hat{\boldsymbol{n}}\times\left[\!\left[\partial_t^j\boldsymbol{E}^n_{h,q}\right]\!\right]\right)\cdot\left(\hat{\boldsymbol{n}}\times\left[\!\left[\partial_t^j\boldsymbol{E}^n_{h,q}\right]\!\right]\right)\\ +\ \bar{Z}^2\left(\hat{\boldsymbol{n}}\times\left[\!\left[\partial_t^j\boldsymbol{H}^n_{h,q}\right]\!\right]\right)\cdot\left(\hat{\boldsymbol{n}}\times\left[\!\left[\partial_t^j\boldsymbol{H}^n_{h,q}\right]\!\right]\right)+\frac{1}{\bar{c}^2}\left(\hat{\boldsymbol{n}}\cdot\left[\!\left[\epsilon\,\partial_t^j\boldsymbol{E}^n_{h,q}\right]\!\right]\right)^2+\bar{c}^2\left(\hat{\boldsymbol{n}}\cdot\left[\!\left[\mu\,\partial_t^j\boldsymbol{H}^n_{h,q}\right]\!\right]\right)^2\mathrm{d}s\,\mathrm{d}t.\end{aligned} \tag{45}$$

Here again the barred coefficients can be taken as averages or values from either side of the interface, and

$$\partial_t^j\boldsymbol{H} = \begin{cases}-\nabla^{j-1}(\nabla\times\boldsymbol{E})/(\epsilon^{\theta-1}\,\mu^\theta), & \text{if } j \text{ odd},\\ -\nabla^{j-2}(\nabla\times\nabla\times\boldsymbol{H})/(\epsilon\,\mu)^{j/2}, & \text{otherwise}.\end{cases} \tag{46}$$

4.3.3. The linear system of equations that solves the optimization problems

For each local patch and for each time step, we solve the following minimization problems

$$\begin{aligned}&\text{Find } (\boldsymbol{H}^n_{h,q},\boldsymbol{E}^n_{h,q})\in V\times V \text{ such that}\\ &\quad(\boldsymbol{H}^n_{h,q},\boldsymbol{E}^n_{h,q}) = \underset{\boldsymbol{v},\boldsymbol{w}\in V}{\arg\min}\,\boldsymbol{J}^n_q(\boldsymbol{v},\boldsymbol{w}),\end{aligned} \tag{47}$$

for the embedded boundary case and

$$\begin{aligned}&\text{Find } (\boldsymbol{H}^{+,n}_{h,q},\boldsymbol{E}^{+,n}_{h,q},\boldsymbol{H}^{-,n}_{h,q},\boldsymbol{E}^{-,n}_{h,q})\in V\times V\times V\times V \text{ such that}\\ &\quad(\boldsymbol{H}^{+,n}_{h,q},\boldsymbol{E}^{+,n}_{h,q},\boldsymbol{H}^{-,n}_{h,q},\boldsymbol{E}^{-,n}_{h,q}) = \underset{\boldsymbol{v}^+,\boldsymbol{w}^+,\boldsymbol{v}^-,\boldsymbol{w}^-\in V}{\arg\min}\,\boldsymbol{J}^n_q(\boldsymbol{v}^+,\boldsymbol{w}^+,\boldsymbol{v}^-,\boldsymbol{w}^-),\end{aligned} \tag{48}$$

for the interface case. Here, in general,

$$V = \{\boldsymbol{v}\in[\mathbb{Q}^k(S_q\times[t_{n-1},t_n])]^3\}, \tag{49}$$

with the obvious reduction in dimensions if TM or TE modes are evolved. We solve the minimization problems (47) and (48) using a procedure similar to that of the one-dimensional case. We therefore compute the matrices of the linear systems of equations, their scaling and LU factorizations as a pre-computation step. The dimension of the matrices is $3\,(k+1)^3$ for problems posed in two space

dimensions and $6(k+1)^4$ in three space dimensions for the embedded boundary case. As for the interface case, the dimension of the matrices is $6(k+1)^3$ in two space dimensions and $12(k+1)^4$ in three space dimensions.

For each update of the numerical solution, we therefore need to compute the right-hand side of the linear systems of equations, solve for the polynomial coefficients and approximate the electromagnetic fields and the required spatial derivatives at the CF nodes using the correction functions. The algorithm of the Hermite-Taylor correction function method to evolve the numerical solution remains the same as the one-dimensional case.

The following propositions guarantee that the minimization problems (47) and (48) are well-posed.

Proposition 1. *The minimization problem (47) has a unique global minimizer.*

Proof. Since we are seeking the correction functions in the polynomial space V, we have

$$\boldsymbol{H}_{h,q}^n = \sum_j c_{q,j}^{H,n} \boldsymbol{\phi}_j \qquad \text{and} \qquad \boldsymbol{E}_{h,q}^n = \sum_j c_{q,j}^{E,n} \boldsymbol{\phi}_j. \tag{50}$$

Here $c_{q,j}^{H,n}$ and $c_{q,j}^{E,n}$ are scalars, and $\boldsymbol{\phi}_j$ are basis functions of the polynomial space V. The quadratic functional J_q^n can therefore be written has

$$J_q^n(\boldsymbol{c}_q^n) = r_q^n + (\boldsymbol{g}_q^n)^T \boldsymbol{c}_q^n + \frac{1}{2}(\boldsymbol{c}_q^n)^T \boldsymbol{M}_q \boldsymbol{c}_q^n. \tag{51}$$

Here $\boldsymbol{c}_q^n$ is a vector containing the coefficients $c_{q,j}^{H,n}$ and $c_{q,j}^{E,n}$ for all j. Let us now verify that M is a positive definite matrix to ensure that we have a global minimizer. Assuming $\boldsymbol{c}_q^n \neq 0$, we notice that

$$\begin{aligned}
\frac{1}{2}(\boldsymbol{c}_q^n)^T \boldsymbol{M}_q \boldsymbol{c}_q^n = \underbrace{\mathcal{G}_q^n(\boldsymbol{H}_{h,q}^n, \boldsymbol{E}_{h,q}^n)}_{\geq 0} + \underbrace{\frac{1}{2}\int_{t_{n-1}}^{t_n}\int_{\partial\Omega\cap S_q} \left(\boldsymbol{n}\times\boldsymbol{E}_{h,q}^n\right)\cdot\left(\boldsymbol{n}\times\boldsymbol{E}_{h,q}^n\right) \mathrm{d}s\,\mathrm{d}t}_{\geq 0} \\
+ \underbrace{\frac{1}{2}\sum_{j=1}^{N_d}\left(\frac{\ell_q}{c}\right)^{2j}\int_{t_{n-1}}^{t_n}\int_{\partial\Omega\cap S_q} \left(\boldsymbol{n}\times\partial_t^j\boldsymbol{E}_{h,q}^n\right)\cdot\left(\boldsymbol{n}\times\partial_t^j\boldsymbol{E}_{h,q}^n\right) \mathrm{d}s\,\mathrm{d}t}_{\geq 0} \\
+ \underbrace{\frac{1}{2}\frac{c_H}{h}\int_{t_{n-\frac{1}{2}}}^{t_n}\int_{S_{p,q}^{\mathcal{H}}} Z^2\boldsymbol{H}_{h,q}^n\cdot\boldsymbol{H}_{h,q}^n + \boldsymbol{E}_{h,q}^n\cdot\boldsymbol{E}_{h,q}^n \,\mathrm{d}\boldsymbol{x}\,\mathrm{d}t}_{>0} + \underbrace{\frac{1}{2}\frac{c_H}{h}\int_{t_{n-1}}^{t_{n-\frac{1}{2}}}\int_{S_{d,q}^{\mathcal{H}}} Z^2\boldsymbol{H}_{h,q}^n\cdot\boldsymbol{H}_{h,q}^n + \boldsymbol{E}_{h,q}^n\cdot\boldsymbol{E}_{h,q}^n \,\mathrm{d}\boldsymbol{x}\,\mathrm{d}t}_{>0},
\end{aligned}$$

since only the zero polynomial can vanish uniformly on $S^{\mathcal{H}_{p,q}}\times[t_{n-1/2},t_n]$ or $S^{\mathcal{H}_{d,q}}\times[t_{n-1},t_{n-1/2}]$. The matrix M_q is therefore positive definite and the minimization problem (47) has a global minimizer. □

Proposition 2. *The minimization problem (48) has a unique global minimizer.*

Proof. The proof is similar to that of Proposition 1. □

Remark 3. The correction function method should preserve the accuracy of the Hermite-Taylor method if $k = 2m$. Let us assume that $k = 2m$ and that polynomials approximating the correction functions have an accuracy of $\mathcal{O}(\ell_i^{k+1})$. Using

$$\begin{aligned}
\boldsymbol{H}_q^n &= \boldsymbol{H} + \mathcal{O}(\ell_q^{k+1}), \\
\boldsymbol{E}_q^n &= \boldsymbol{E} + \mathcal{O}(\ell_q^{k+1}),
\end{aligned} \tag{52}$$

in the functional J_q^n we obtain that all terms in the functional J_q^n scale as $\mathcal{O}(\ell_q^{2k+5})$. This is also consistent with the dimensional analysis made in Remark 1. Here J_q^n is either given by (17) for an embedded boundary problem or (30) for an interface problem. We require that $c_H > 0$ to have a well-posed minimization problem. We also require that $c_H \leq 1$ so that the Hermite functionals are not dominating the Maxwell's equations residuals and the boundary or interface conditions in J_q^n. We choose $c_H = 1$ since the condition number of the matrices M_q scales as $\mathcal{O}(c_H^{-1})$, as shown in [18].

Remark 4. Taking $k = 2m$, the computational cost of the CFM is not negligible and increases as m increases because the dimension of the matrices scales as $(2m+1)^3$ and $(2m+1)^4$ in respectively two and three space dimensions. Fortunately, for a given time step, the minimization problems are independent and therefore can be solved in parallel, reducing the computational cost of the CFM. Note that the pre-computation step of the CFM (computation of the matrices M_i, their scaling and LU factorizations) can also be performed in parallel. We refer the reader to [30] for more information about the benefits of a parallel implementation of the CFM.

5. Numerical examples

In this section, we numerically investigate the stability of the Hermite-Taylor correction function method and perform convergence studies in one and two space dimensions.

5.1. Hermite-Taylor correction function methods in one dimension

We consider the 1-D simplification of Maxwell's Eq. (15). For a $(2m+1)$-order Hermite-Taylor method, we use polynomials of degree $2m$ as the correction functions to maintain accuracy and choose $c_H = 1$. The physical parameters are $\mu = 1$ and $\epsilon = 1$.

5.1.1. Stability

The first example considers a domain where all the CF nodes belong to the primal mesh. This allows us to write the Hermite-Taylor correction function method as a one step method for the solution on the primal nodes since the Hermite functionals for the primal CF nodes only require the numerical solutions at times t_n and $t_{n+1/2}$ to evolve the data from t_n to t_{n+1}. In this situation, we express as a one-step method

$$\boldsymbol{W}^{n+1} = A\,\boldsymbol{W}^{n}. \tag{53}$$

Here $\boldsymbol{W}^n$ contains all the degrees of freedom on the primal mesh at time t_n and A is a square matrix of dimension $2(m+1)(N_x+1)$. A stable method should have all the eigenvalues of A on or inside the unit circle. We then compute the spectral radius of A, denoted as $\rho(A)$. Note that this is only a necessary condition. That being said, the stability properties of the method are also corroborated by the results of long time simulations presented at the end of this subsection. We consider the physical domain $\Omega = [h_{\max} - \frac{h_{\min}}{3}, 1 - h_{\max} + \frac{5h_{\min}}{12}]$ and the computational domain $\Omega_c = [0,1]$. Here $h \in \{\frac{1}{25}, \frac{1}{50}, \frac{1}{100}, \frac{1}{200}, \frac{1}{400}, \frac{1}{800}, \frac{1}{1600}\}$.

The absolute difference between $\rho(A)$ and one is illustrated in Fig. 10 for different mesh sizes, CFL constants and values of N_d, that is the maximum order of the derivatives in the functional $\mathcal{B}$ (22). Note that we consider the spatial derivatives of the correction functions in the functional $\mathcal{B}$. In other words, we convert the time derivatives of the electromagnetic fields in the functional $\mathcal{B}$ using the relations (21). We consider that the method is stable if the spectral radius $\rho(A)$ is at most one with an error of $\mathcal{O}(10^{-10})$.

According to the numerical results, the stability of the method improves as either the CFL constant decreases, the value N_d increases or the mesh size decreases. Note that the CFL constant under which the method is stable increases as the mesh size decreases or the value N_d increases. Moreover, for $m = 1-2$ and $N_d = m$, we recover the stability condition of the original Hermite-Taylor method (CFL = 1). Although the same behaviour is observed for $m = 4$, the difference between $\rho(A)$ and one is larger, particularly for $N_d \geq 5$. This can be partly explained by the large condition number of the CFM matrices (see Section 5.1.2) that prevents an accurate approximation of the matrix A and therefore of its spectral radius.

The stability of the proposed Hermite-Taylor correction function method can also be further improved by the Hermite smoothing step suggested in [17]. Note that we do not need to update the CF nodes at each iteration of the smoothing step. We repeated the same numerical examples but with one and ten iterations of the Hermite smoothing step at the end of each time step. The numerical results suggest that increasing N_d has a much greater impact on the stability.

We now perform the same test but this time we use directly the time derivatives of the electromagnetic fields in the functional $\mathcal{B}$ instead of converting them into spatial derivatives, leading to a method that is easier to implement. By consistency, this would also implicitly penalize the spatial derivatives and therefore we should expect an improvement of the stability condition. The absolute difference between $\rho(A)$ and one is illustrated in Fig. 11 for different mesh sizes, CFL constants and values of N_d, that is the maximum order of the time derivatives that are considered in the functional $\mathcal{B}$ (22). For all values of m, there is a clear improvement when N_d goes from 0 to 1. However, for $N_d > 1$, there is no significant improvement of the stability of the method when compared with $N_d = 1$. For $m = 4$ and $N_d \geq 5$, we even observe a deterioration of the stability of the method. We therefore always convert time derivatives of the variable fields into spatial derivatives since this leads to a Hermite-Taylor correction function method that is stable for a larger CFL constant.

Let us now consider a domain where there are primal and dual CF nodes. The physical domain $\Omega = [\frac{\pi}{50}, 1 - \frac{\pi}{100}]$ while the computational domain is $\Omega_c = [0,1]$. In this situation, to express the method as a one-step evolution we would have to include both the primal and dual node solutions in the definition of $\boldsymbol{W}^n$ in (53). Instead we here investigate the stability using long time simulations. We consider the trivial solution for all electromagnetic fields but with initial data, namely the electromagnetic fields and their first m derivatives, to be random numbers in $(-10\,\epsilon_m, 10\,\epsilon_m)$. Here ϵ_m is the machine precision.

Fig. 12 illustrates the maximum norm of the numerical solution over 10^6 time steps as a function of the CFL constant for different mesh sizes and values of N_d. Here again, the stability of the Hermite-Taylor correction function methods improves as either the CFL constant decreases, the value N_d increases or the mesh size decreases. For $m = 1,2,3$ with respectively $N_d = 0,1,4$, we recover the stability condition of the original Hermite-Taylor method (CFL = 1).

5.1.2. Condition number of correction function matrices

In this subsection, we investigate the condition number of the correction function matrices coming from the minimization procedure. We consider the numerical example where only primal CF nodes are needed with the same settings as previously described. Fig. 13 illustrates the maximum condition number of the CF matrices as a function of the CFL for different mesh sizes and values of N_d. We observe that the condition number of the matrices M increases as N_d increases. Note that the condition number of the

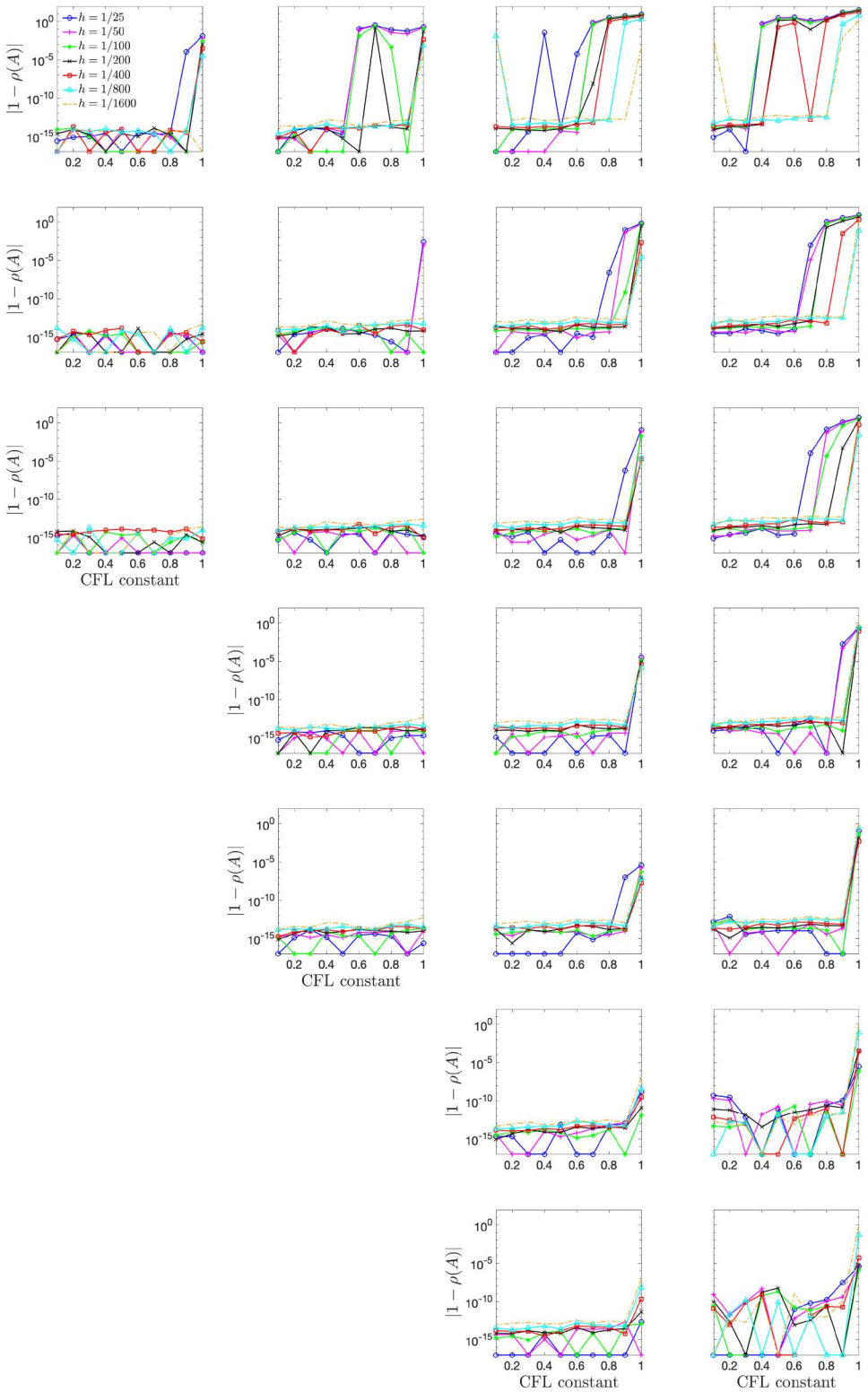

Fig. 10. Absolute difference between one and the spectral radius $\rho(A)$ of the matrix A as a function of the CFL constant for different mesh sizes using the constraints on spatial derivatives. The columns are for different m: 1 to 4 from the left to the right. The rows are for the maximum order of the considered spatial derivatives (N_d) at the boundary: 0 to 6 from the top to the bottom.

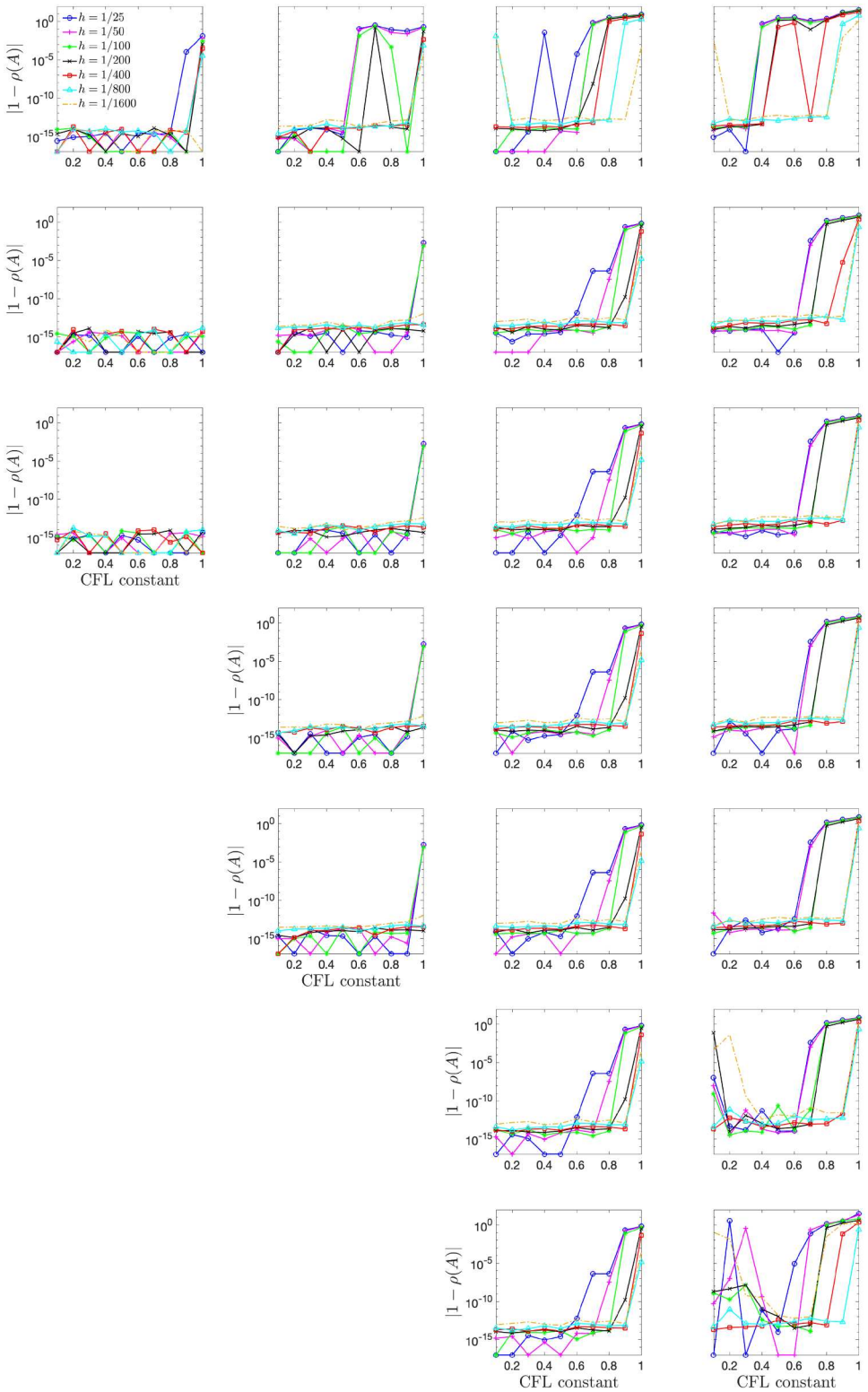

Fig. 11. Absolute difference between one and the spectral radius $\rho(A)$ of the matrix A as a function of the CFL constant for different mesh sizes using the constraints on the time derivatives. The columns are for different m: 1 to 4 from the left to the right. The rows are for the maximum order of the considered time derivatives (N_d) at the boundary: 0 to 6 from the top to the bottom.

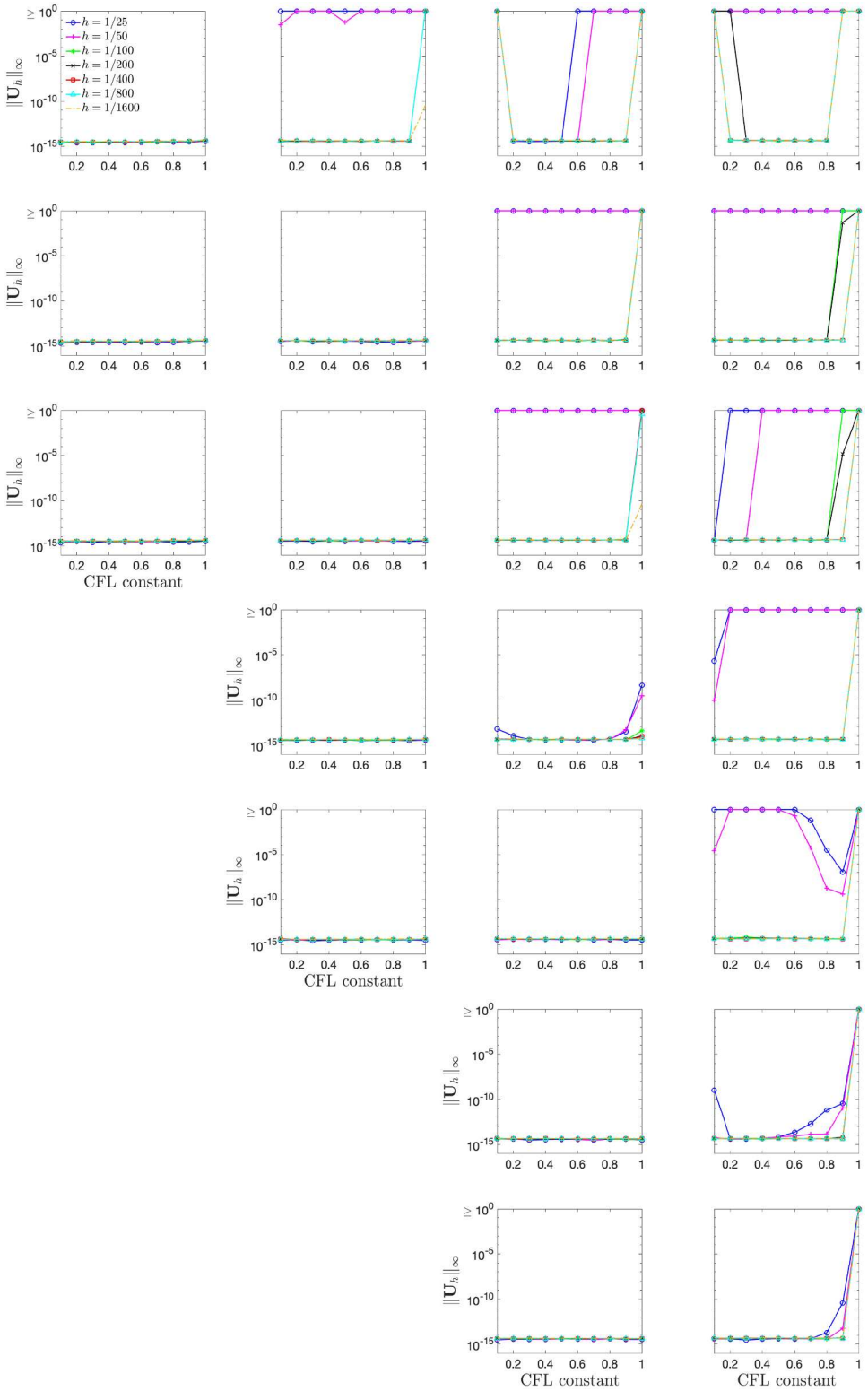

Fig. 12. Maximum value of the maximum norm of the numerical solution over 10^6 time steps as a function of the CFL constant for different mesh sizes. The columns are for different m: 1 to 4 from the left to the right. The rows are for the maximum order of the considered spatial derivatives (N_d) at the boundary: 0 to 6 from the top to the bottom.

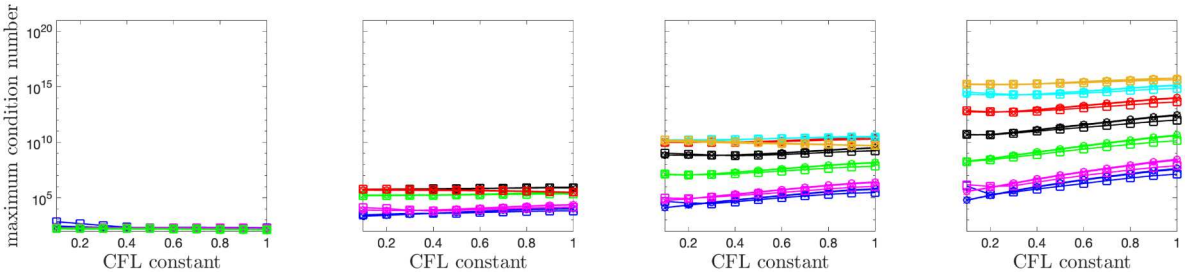

Fig. 13. Maximum condition number of CF matrices as a function of the CFL constant for different mesh sizes and number of spatial derivatives at the boundary. The value m is 0 to 4 from the left to the right. The circle, cross and square markers stand for $\Delta x = \frac{1}{25}$, $\Delta x = \frac{1}{200}$ and $\Delta x = \frac{1}{1600}$. The colors blue, magenta, green, black, red, cyan and orange are respectively for $N_d = 0 - 6$. (For interpretation of the references to colour in this figure legend, the reader is referred to the web version of this article.)

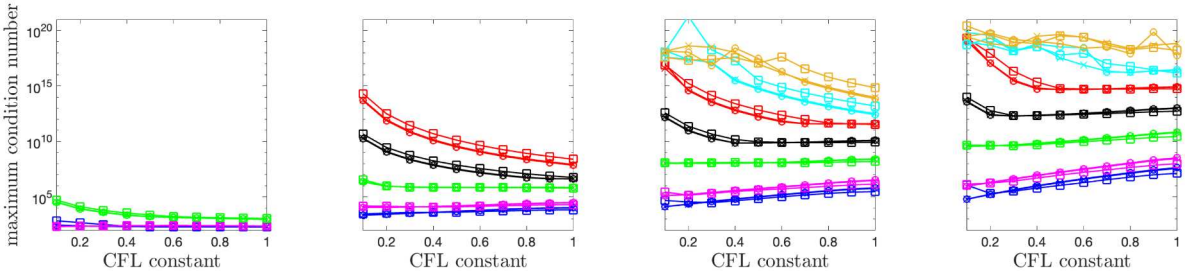

Fig. 14. Maximum condition number of CF matrices as a function of the CFL constant for different mesh sizes and number of time derivatives at the boundary. The value m is 0 to 4 from the left to the right. The circle, cross and square markers stand for $\Delta x = \frac{1}{25}$, $\Delta x = \frac{1}{200}$ and $\Delta x = \frac{1}{1600}$. The colors blue, magenta, green, black, red, cyan and orange are respectively for $N_d = 0 - 6$. (For interpretation of the references to colour in this figure legend, the reader is referred to the web version of this article.)

CF matrices remains roughly constant with respect to the CFL constant for $m \leq 2$. For $m = 3$ and $m = 4$, it decreases when the CFL constant diminishes.

Fig. 14 illustrates the condition number of the CF matrices as a function of the CFL constant for different meshes and N_d when the time derivatives are directly considered in the functional B. The condition number increases when N_d increases and, for $N_d > 2$, when the CFL constant diminishes. Note that, when we convert the time derivatives of the electromagnetic fields into spatial derivatives, it leads to better conditioned CF matrices. This further motivates us to convert time derivative of the electromagnetic fields used in the boundary (or interface) conditions into spatial derivatives.

5.1.3. Accuracy

Let us now investigate the accuracy of the Hermite-Taylor correction function method with $m = 1 - 4$. The physical parameters are $\mu = 1$ and $\epsilon = 1$. We set $\Delta t = 0.9\,h$ for $m \leq 3$ and $N_d = 0, 2, 5$ for respectively $m = 1, 2, 3$. For $m = 4$, we use $\Delta t = 0.8\,h$ and $N_d = 3$. The physical domain is $\Omega = [\frac{\pi}{50}, 1 - \frac{\pi}{100}]$ while the computational domain is $\Omega_c = [0, 1]$. The time interval is $I = [0, 20]$. The initial and boundary conditions are chosen so that the solution to Maxwell's equations is

$$\begin{aligned} H(x,t) &= \sin(250\,x)\,\sin(250\,t), \\ E(x,t) &= \cos(250\,x)\,\cos(250\,t). \end{aligned} \tag{54}$$

The relative error in the L^2-norm is computed at the final time. Fig. 15 illustrates the convergence plots for $m = 1 - 4$. We observe a rough $2\,m + 1$ convergence order for all values of m.

5.2. Hermite-Taylor correction function methods in two dimensions

We consider the two-dimensional simplification of Maxwell's Eq. (7). The correction function polynomials are chosen to be elements of $\mathbb{Q}^{2\,m}$ to preserve the accuracy of the Hermite-Taylor method and we choose $c_H = 1$. We set $\Delta L_\Gamma = \alpha h$ with $\alpha = 1.5$ for the local patches.

Considering an interface problem with two different media, the L^2-norm of the divergence of the magnetic field at the final time is computed using

$$\|\nabla \cdot (\mu \boldsymbol{H}_h)\|_2 = \|\nabla \cdot (\mu \boldsymbol{H}^*)\|_2 + \sum_{q=0}^{N_{cf}-1} \left(\|\nabla \cdot (\mu \boldsymbol{H}^+_{h,q})\|_2 + \|\nabla \cdot (\mu \boldsymbol{H}^-_{h,q})\|_2 \right). \tag{55}$$

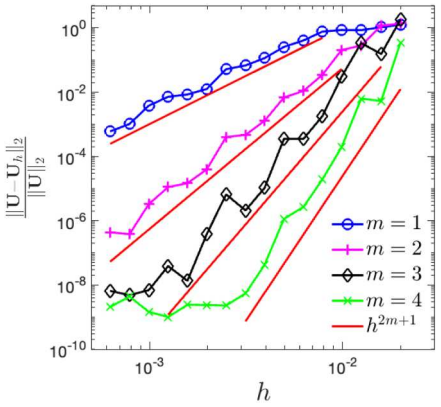

Fig. 15. Convergence plots for embedded boundary problems using the Hermite-Taylor correction function method with $1 \leq m \leq 4$ at final time $t_f = 20$. Here $\mathbf{U} = [H, E]^T$.

Here N_{cf} is the number of patches required for the CFM, $\boldsymbol{H}^*$ is the approximation of the magnetic field coming from the Hermite-Taylor method, and $\boldsymbol{H}^{\pm}_{h,q}$, $q = 0, \ldots, N_{cf} - 1$, are the CF magnetic field approximations associated with the subdomain $\Omega^{\pm}$. The first term in (55) computes the L^2-norm of the divergence of magnetic field approximation coming from the Hermite-Taylor numerical solution. Since the Hermite-Taylor cells do not cover a narrow band around the interface, as shown in Fig. 9, we also consider the contribution of the divergence of the magnetic field approximations coming from the correction function method. The second term therefore sums the L^2-norm of the divergence of the CF magnetic field on each local patch.

5.2.1. Stability

In this subsection, we investigate the stability of the Hermite-Taylor correction function method for embedded boundary and interface problems. To do so, we use long time simulations. We first consider an embedded boundary problem. The computational domain is $\Omega_c = [0, 1] \times [0, 1]$ and the embedded boundary Γ is a circle with a radius of 0.3 and centered at $(0.5, 0.5)$ that encloses the physical domain Ω. As in the one-dimensional experiments described above, we consider the trivial solution for all electromagnetic fields but with initial data, namely the electromagnetic fields and the necessary derivatives, to be random numbers in $(-10\,\epsilon_m, 10\,\epsilon_m)$. The physical parameters are set to $\mu = 1$ and $\epsilon = 1$.

Fig. 16 illustrates the evolution of the maximum norm of the numerical solution over 10^5 time steps for $m = 1 - 2$ using different mesh sizes, values of N_d and CFL constants.

For $m = 1$, the Hermite-Taylor correction function method is stable for all considered mesh sizes and CFL constants when $N_d = 2$, the maximum value of N_d in this situation. As for $m = 2$, the stability of the Hermite-Taylor correction function method is clearly improving as N_d increases. More specifically, the method for $m = 2$ is stable for all considered meshes when the CFL constant is smaller than 0.8 and $N_d \geq 2$.

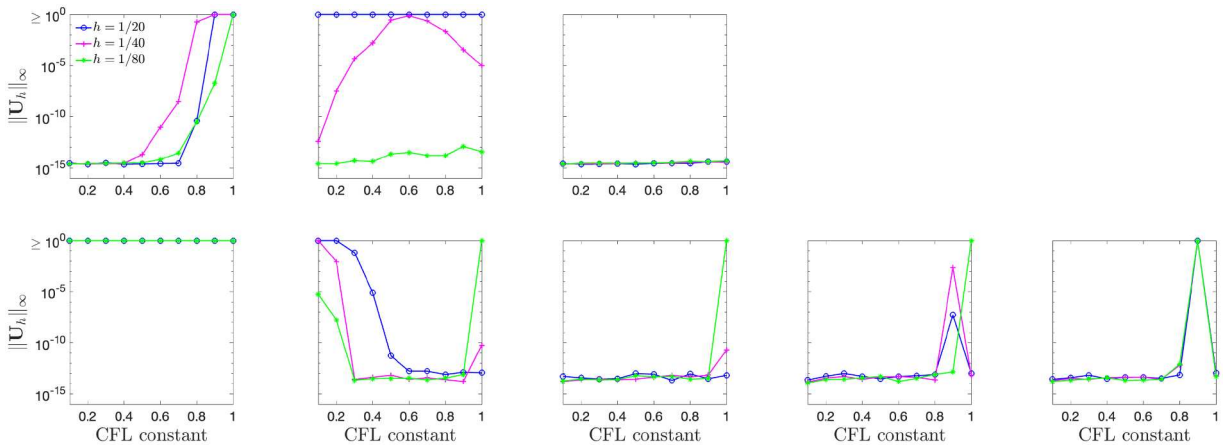

Fig. 16. Maximum value of the maximum norm of the numerical solution over 10^5 time steps as a function of the CFL constant for different mesh sizes in 2-D for PEC boundary conditions. The rows are for different m: 1 to 2 from the top to bottom. The columns are for the maximum order of the considered spatial derivatives (N_d) at the boundary: 0 to 4 from the left to the right.

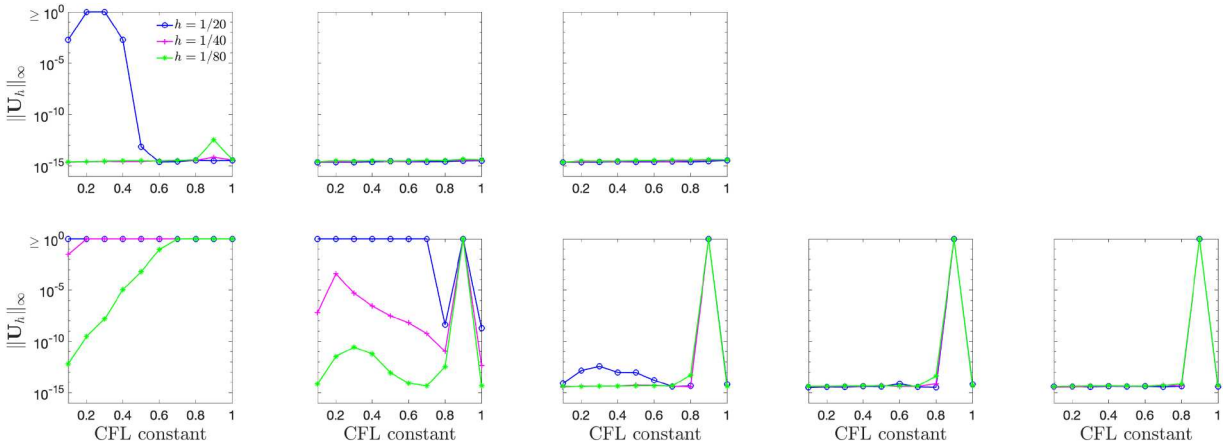

Fig. 17. Maximum value of the maximum norm of the numerical solution over 10^5 time steps as a function of the CFL constant for different mesh sizes in 2-D for interface conditions. The rows are for different m: 1 to 2 from the top to bottom.The columns are for the maximum order of the considered spatial derivatives (N_d) at the boundary: 0 to 4 from the left to the right.

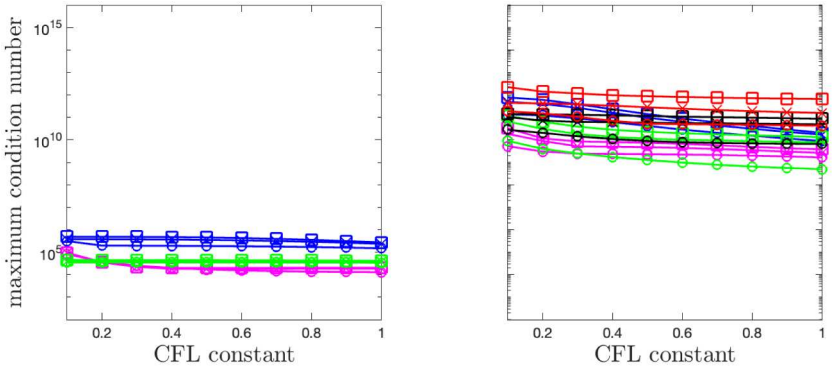

Fig. 18. Maximum condition number of CF matrices as a function of the CFL constant for different mesh sizes and number of derivatives in 2-D for PEC boundary conditions. The left and right plots illustrate the results for respectively $m = 1$ and $m = 2$. The circle, cross and square markers stand for $\Delta x = \frac{1}{25}$, $\Delta x = \frac{1}{200}$ and $\Delta x = \frac{1}{1600}$. The colors blue, magenta, green, black and red are respectively for $N_d = 0 - 4$. (For interpretation of the references to colour in this figure legend, the reader is referred to the web version of this article.)

Let us now consider interface problems. We investigate the stability using the same setup as for the embedded boundary problems. In this situation, the domain is $\Omega = [0, 1] \times [0, 1]$, Γ is an interface and the subdomain Ω^+ is enclosed by Γ. We consider periodic boundary conditions. We are seeking a numerical solution in Ω^+ and Ω^-. We consider $\mu^+ = 1$, $\epsilon^+ = 1$, $\mu^- = 2$ and $\epsilon^- = 2.25$.[1] Fig. 17 illustrates the evolution of the maximum norm of the numerical solution over 10^5 time steps for $m = 1 - 2$ using different mesh sizes, values of N_d and CFL constants. For $m = 1$ and $N_d \geq 1$, the Hermite-Taylor correction function method is stable for all considered CFL constants. Regarding $m = 2$, the method is stable for $N_d \geq 3$ and a CFL constant under 0.8.

5.2.2. *Condition number of correction function matrices*

We first investigate the condition number of the CF matrices for the embedded boundary problem described previously. The maximum condition number of CFM matrices as a function of the CFL constant for different mesh sizes and values of N_d is illustrated in Fig. 18. As in the one space dimension case, the condition number increases as m increases. For $m = 2$, the condition number increases when the CFL constant diminishes, suggesting that we should choose the largest CFL constant that leads to a stable method. As for N_d, we observe that the CFM matrices are better conditioned when N_d goes from 0 to 1. However, for $N_d > 1$, the condition number increases as N_d increases. For $m = 2$, we notice that the condition number increases as the mesh size decreases.

Let us now consider the interface problem described in the previous subsection. Fig. 19 illustrates the condition number of the CFM matrices as a function of the CFL constant for different meshes and values of N_d. For $m = 1$, we observe an improvement of the condition number when N_d goes from 0 to 1 but it increases as the CFL constant diminishes for $N_d = 0 - 1$. For $m = 2$ and $N_d < 3$, the condition number diminishes as N_d increases while it increases as the CFL constant diminishes. For $m = 2$ and $N_d = 4$, the condition number decreases as the CFL decreases.

[1] Note that we set $Z^+ = Z^- = 1$ and $c^+ = c^- = 1$ in the correction function functional for all numerical examples in this work.

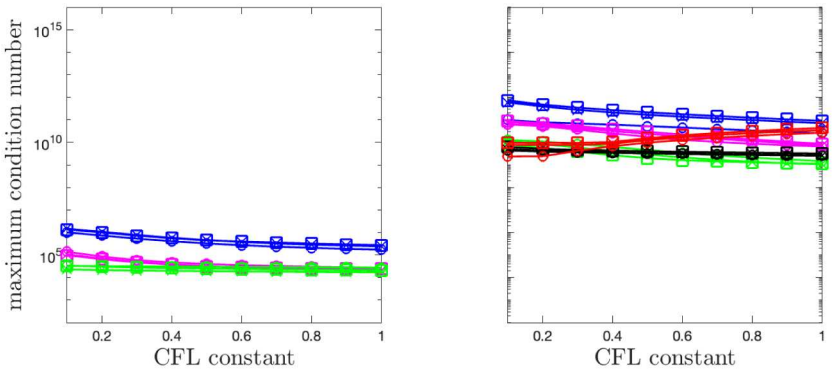

Fig. 19. Maximum condition number of CF matrices as a function of the CFL constant for different mesh sizes and number of derivatives in 2-D for interface conditions. The left and right plots illustrate the results for respectively $m = 1$ and $m = 2$. The circle, cross and square markers stand for $\Delta x = \frac{1}{25}$, $\Delta x = \frac{1}{200}$ and $\Delta x = \frac{1}{1600}$. The colors blue, magenta, green, black and red are respectively for $N_d = 0 - 4$. (For interpretation of the references to colour in this figure legend, the reader is referred to the web version of this article.)

Due to the condition number of the CF matrices, we limit the value of m to 2 in the multi-dimensional case. Nevertheless, we obtain third-order and fifth-order Hermite-Taylor correction function methods that are stable under a CFL constant of around 1 and 0.8 respectively. Future research will explore a collocation method, similar to what is done in [31], to obtain better conditioned linear systems for the correction functions and therefore to consider larger values of m.

5.2.3. Accuracy

Let us now investigate the accuracy of the Hermite-Taylor correction function method. Since the degree of the correction function polynomials is $2m$, we should expect third and fifth order convergence, respectively, for Hermite-Taylor correction function methods with $m = 1$ and $m = 2$. We use a CFL constant of 0.9 and 0.7 for the third and fifth order Hermite-Taylor correction function methods.

Embedded Boundary Problems

We first consider the computational domain $\Omega_c = [-0.1, 1.1] \times [-0.1, 1.1]$, illustrated in Fig. 20, and the time interval is $I = [0, 1]$. In this situation, we are seeking a numerical solution in Ω^+, enclosed by Γ_1 and Γ_2. The physical parameters are $\mu = 1$ and $\epsilon = 1$. The initial data, and boundary conditions on Γ_1 and Γ_2 are chosen so that the solution in Ω^+ is given by

$$\begin{aligned} H_x &= -\frac{1}{\sqrt{2}} \sin(\omega \pi x) \cos(\omega \pi y) \sin(\sqrt{2}\,\omega \pi t), \\ H_y &= \frac{1}{\sqrt{2}} \cos(\omega \pi x) \sin(\omega \pi y) \sin(\sqrt{2}\,\omega \pi t), \\ E_z &= \sin(\omega \pi x) \sin(\omega \pi y) \cos(\sqrt{2}\,\omega \pi t), \end{aligned} \tag{56}$$

where $\omega = 20$. Figs. 21 and 22 show the convergence plots of the electromagnetic fields and the divergence of the magnetic field in the L^2-norm for $m = 1$ and $m = 2$.

For $m = 1$, we set $N_d = 2$ so that the method is stable and we observe a clear third-order convergence for the electromagnetic fields and second-order convergence for the divergence of the magnetic field, as expected. As for $m = 2$, we consider $N_d = 2 - 4$, leading to a stable method when the CFL constant is 0.7. When $N_d = 2$, we observe a clear fifth-order convergence for the electromagnetic fields

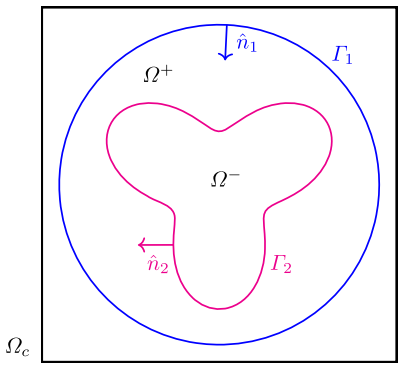

Fig. 20. Geometry of the computational domain Ω_c.

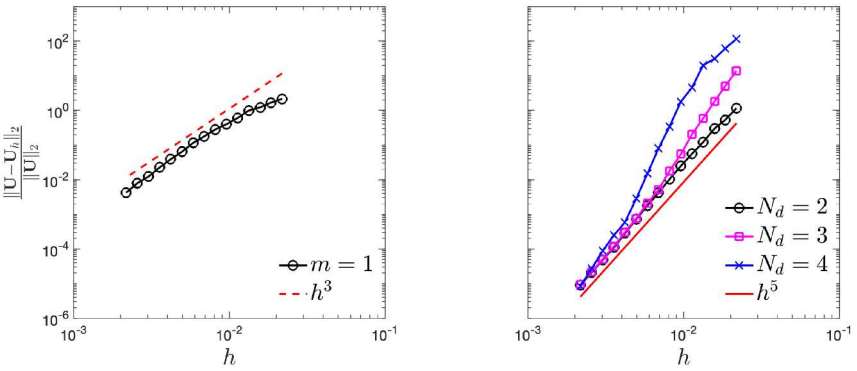

Fig. 21. Convergence plots for an embedded boundaries problem with the geometry illustrated in Fig. 20 using the third and fifth order Hermite-Taylor correction function methods. The left and right plots illustrate the results for respectively $m = 1$ and $m = 2$. Here $\mathbf{U} = [H_x, H_y, E_z]^T$.

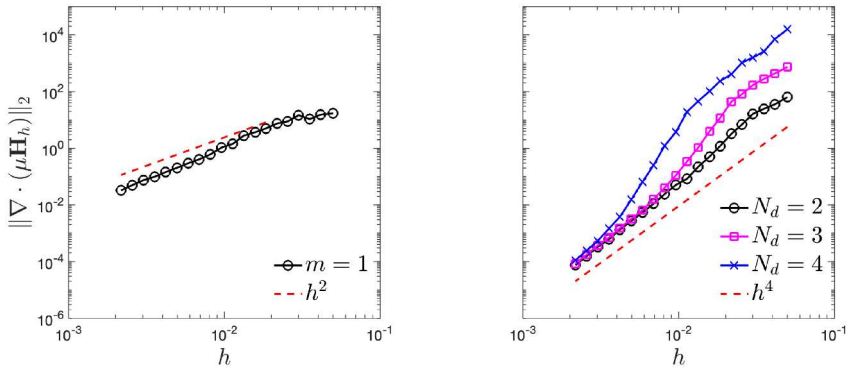

Fig. 22. Convergence plots of the divergence of the magnetic field for an embedded boundaries problem with the geometry illustrated in Fig. 20 using the third and fifth order Hermite-Taylor correction function methods. The left and right plots illustrate the results for respectively $m = 1$ and $m = 2$.

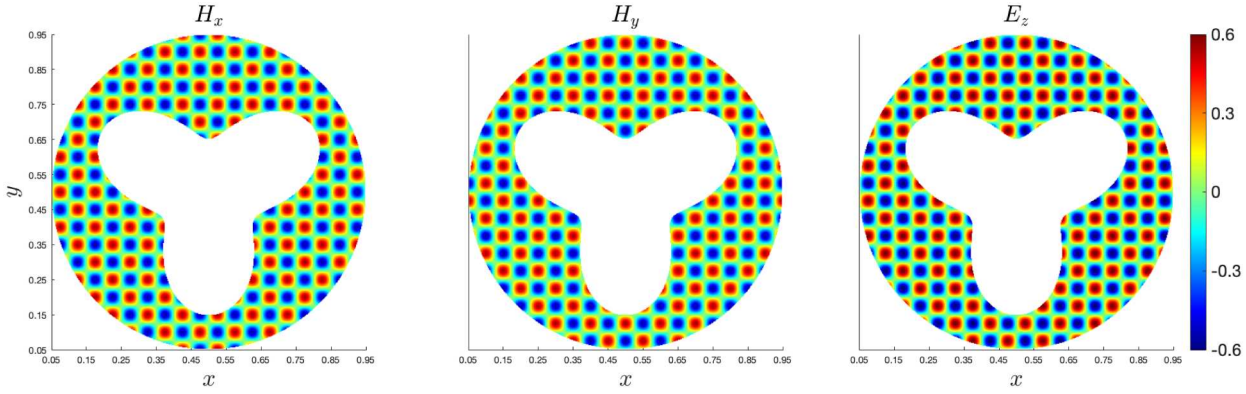

Fig. 23. The components H_x, H_y and E_z at the final time $t_f = 1$ for an embedded boundary problem with the geometry illustrated in Fig. 20 using the fifth-order Hermite-Taylor correction function method and $h = \frac{1}{460}$.

and fourth-order for $\nabla \cdot (\mu \boldsymbol{H}_h)$. However, as N_d increases, the relative error also increases and this makes the method inaccurate for coarser meshes. Note that the boundary condition (3) varies in space and time, and enforces a standing wave with a wavelength of 0.1. In this situation, for coarser meshes, it is more challenging for the minimization problem to provide accurate correction functions, particularly when we consider additional constraints on the spatial derivatives. The approximations of electromagnetic fields at the final time are illustrated in Fig. 23.

For the remaining examples in this work, we set N_d to 2 and 4 for respectively $m = 1$ and $m = 2$.

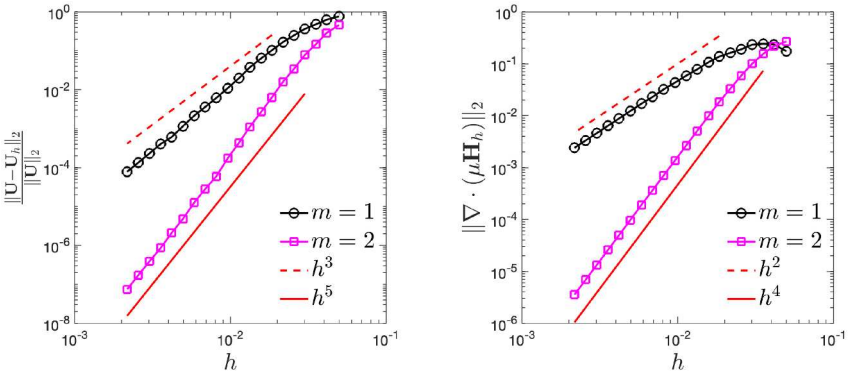

Fig. 24. Convergence plots for a circular cavity problem using the third and fifth order Hermite-Taylor correction function methods. The left and right plots show the convergence of the electromagnetic fields and the divergence of the magnetic fields. Here $\mathbf{U} = [H_x, H_y, E_z]^T$.

Let us now consider a circular cavity problem. The computational domain is $\Omega_c = [-1.1, 1.1] \times [-1.1, 1.1]$ and the embedded boundary Γ is a circle of unit radius and centered at $(0, 0)$ that encloses the physical domain Ω. The time interval is $I = [0, 1]$ and we enforce PEC boundary conditions on Γ. The physical parameters are $\epsilon = 1$ and $\mu = 1$, and the solution in cylindrical coordinates in Ω is given by

$$\begin{aligned} H_\rho(\rho, \phi, t) &= \frac{i}{\alpha_{i,j}\, \rho}\, J_i(\alpha_{i,j}\, \rho)\, \sin(i\, \phi)\, \sin(\alpha_{i,j}\, t), \\ H_\phi(\rho, \phi, t) &= \frac{1}{2} \left(J_{i-1}(\alpha_{i,j}\, \rho) - J_{i+1}(\alpha_{i,j}\, \rho) \right) \cos(i\, \phi)\, \sin(\alpha_{i,j}\, t), \\ E_z(\rho, \phi, t) &= J_i(\alpha_{i,j}\, \rho)\, \cos(i\, \phi)\, \cos(\alpha_{i,j}\, t), \end{aligned} \tag{57}$$

where $\alpha_{i,j}$ is the jth positive real root of the i-order Bessel function of first kind J_i, $i = 2$ and $j = 11$. The left plot of Fig. 24 shows that we obtain the expected $2\,m + 1$ rates of convergence for the electromagnetic fields in the L^2-norm. The $2\,m$ rates of convergence for the divergence of the magnetic field are illustrated in the right plot of Fig. 24. Fig. 25 illustrates the approximations of electromagnetic fields at the final time.

Interface Problems with Analytic Solutions

Let us now consider Maxwell's interface problems. First, we consider a dielectric cylinder in free-space exposed to an excitation wave. The geometry of the computational domain consists of two concentric circles enclosed in $\Omega_c = [-1, 1] \times [-1, 1]$. The first circle centered at $(0, 0)$ has a radius of 0.8 and is an embedded boundary Γ_1 of Ω^+. The second circle also centered at $(0, 0)$, but with a radius $r_0 = 0.6$, which represents the interface Γ_2 between the subdomains and enclosed the subdomain Ω^-. The time interval is set to $I = [0, 1]$. The initial and boundary conditions are chosen such that the solution in cylindrical coordinates is given by the real part

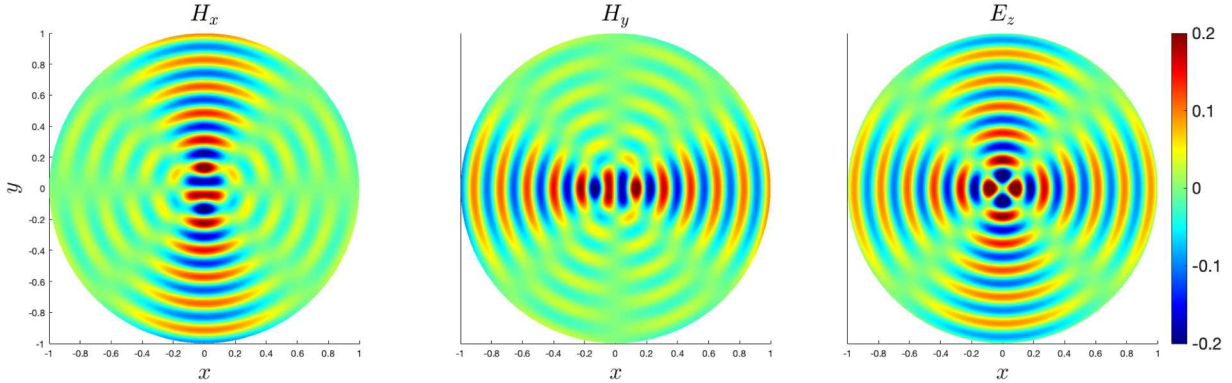

Fig. 25. The components H_x, H_y and E_z at the final time $t_f = 1$ for a circular cavity problem using the fifth-order Hermite-Taylor correction function method and $h = \frac{1}{460}$.

of

$$
H_\theta(r,\theta,t) = \begin{cases} -\frac{\mathrm{i}\,k^-}{\omega\,\mu^-} \sum_{n=-\infty}^{\infty} C_n^{\mathrm{tot}}\, J_n'(k^- r)\, e^{\mathrm{i}\,(n\theta+\omega t)}, & \text{if} \quad r \le r_0, \\ -\frac{\mathrm{i}\,k^+}{\omega\,\mu^+} \sum_{n=-\infty}^{\infty} (\mathrm{i}^{-n} J_n'(k^+ r) + C_n^{\mathrm{scat}}\, H_n^{(2)'}(k^+ r))\, e^{\mathrm{i}\,(n\theta+\omega t)}, & \text{if} \quad r > r_0, \end{cases}
$$

$$
H_r(r,\theta,t) = \begin{cases} -\frac{1}{\omega\,\mu^- r} \sum_{n=-\infty}^{\infty} n\, C_n^{\mathrm{tot}}\, J_n(k^- r)\, e^{\mathrm{i}\,(n\theta+\omega t)}, & \text{if} \quad r \le r_0, \\ -\frac{1}{\omega\,\mu^+ r} \sum_{n=-\infty}^{\infty} n\,(\mathrm{i}^{-n} J_n(k^+ r) + C_n^{\mathrm{scat}}\, H_n^{(2)}(k^+ r))\, e^{\mathrm{i}\,(n\theta+\omega t)}, & \text{if} \quad r > r_0, \end{cases} \tag{58}
$$

$$
E_z(r,\theta,t) = \begin{cases} \sum_{n=-\infty}^{\infty} C_n^{\mathrm{tot}}\, J_n(k^- r)\, e^{\mathrm{i}\,(n\theta+\omega t)}, & \text{if} \quad r \le r_0, \\ \sum_{n=-\infty}^{\infty} (\mathrm{i}^{-n} J_n(k^+ r) + C_n^{\mathrm{scat}}\, H_n^{(2)}(k^+ r))\, e^{\mathrm{i}\,(n\theta+\omega t)}, & \text{if} \quad r > r_0, \end{cases}
$$

with

$$
\begin{aligned} C_n^{\mathrm{tot}} &= \mathrm{i}^{-n} \frac{\frac{k^+}{\mu^+}\,(J_n'(k^+ r_0)\, H_n^{(2)}(k^+ r_0) - H_n^{(2)'}(k^+ r_0)\, J_n(k^+ r_0))}{\frac{k^-}{\mu^-}\, J_n'(k^- r_0)\, H_n^{(2)}(k^+ r_0) - \frac{k^+}{\mu^+}\, H_n^{(2)'}(k^+ r_0)\, J_n(k^- r_0)}, \\ C_n^{\mathrm{scat}} &= \mathrm{i}^{-n} \frac{\frac{k^+}{\mu^+}\, J_n'(k^+ r_0)\, J_n(k^- r_0) - \frac{k^-}{\mu^-}\, J_n'(k^- r_0)\, J_n(k^+ r_0)}{\frac{k^-}{\mu^-}\, J_n'(k^- r_0)\, H_n^{(2)}(k^+ r_0) - \frac{k^+}{\mu^+}\, H_n^{(2)'}(k^+ r_0)\, J_n(k^- r_0)}. \end{aligned} \tag{59}
$$

Here $\omega = 2\,\pi$, $k^\circ = \omega\,\sqrt{\mu^\circ\,\epsilon^\circ}$, J_n is the n-order Bessel function of first kind and $H_n^{(2)}$ is the n-order Hankel function of second kind and the imaginary number is i [3,32]. We set $\mu^+ = 1$, $\epsilon^+ = 1$, $\mu^- = 2$ and $\epsilon^- = 2.25$. Hence, Ω^- is a magnetic dielectric material. In this situation, H_x and H_y are discontinuous at the interface and E_z is continuous.

As shown in Fig. 26, we observe the expected $2\,m+1$ and $2\,m$ rates of convergence for respectively the electromagnetic fields and the divergence of the magnetic field, even in the presence of discontinuities.

The approximations of electromagnetic fields at the final time are illustrated in Fig. 27.

Fig. 28 illustrates the magnetic field components at $y = 0.2$ along x.

The discontinuities at the interface are well captured by the Hermite-Taylor correction function method.

Interface Problems with Reference Solutions

We consider the computational domain illustrated in Fig. 20 with $\Omega_c = [0,1]\times[0,1]$ and a time interval $I = [0,1]$. We set $\mu^+ = 1$, $\epsilon^+ = 1$, $\mu^- = 2$ and $\epsilon^- = 2.25$ so H_x and H_y could be discontinuous at the interface. The boundary condition on Γ_1 is given by

$$
E_z(t) = e^{-\frac{(t-0.3)^2}{2\,\sigma^2}}, \tag{60}
$$

while interface conditions (6) are enforced on Γ_2. Here $\sigma = 0.02$. The initial conditions are given by trivial electromagnetic fields. To our knowledge, there is no analytical solution to this problem. Hence, we compute a reference solution $\boldsymbol{U}^*$ using a Richardson

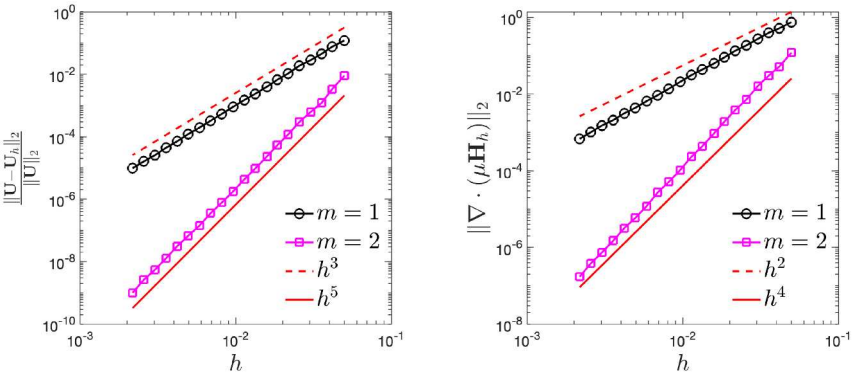

Fig. 26. Convergence plots for the scattering of a magnetic dielectric cylinder problem using the third and fifth order Hermite-Taylor correction function methods. The left and right plots show the convergence of the electromagnetic fields and the divergence of the magnetic fields. Here $\mathbf{U} = [H_x, H_y, E_z]^T$.

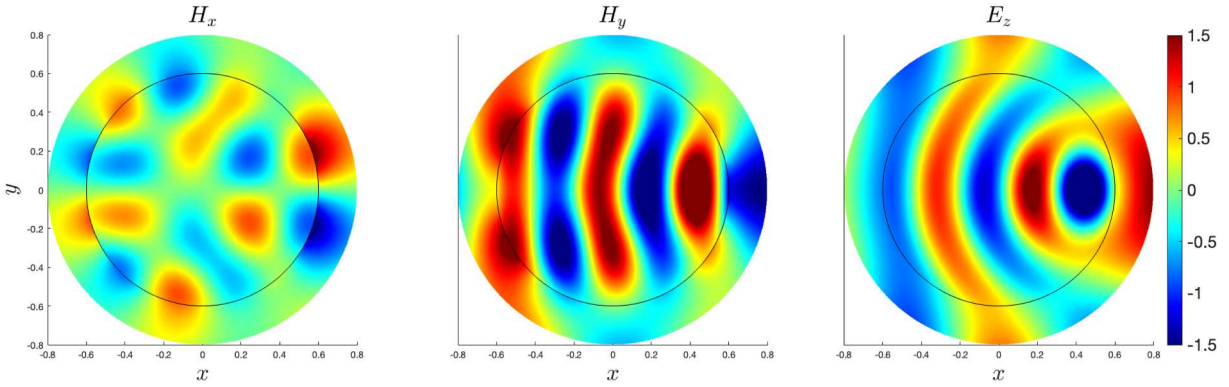

Fig. 27. The components H_x, H_y and E_z at the final time $t_f = 1$ for the scattering of a magnetic dielectric problem using the fifth-order Hermite-Taylor correction function method and $h = \frac{1}{460}$. The interface is represented by the black line.

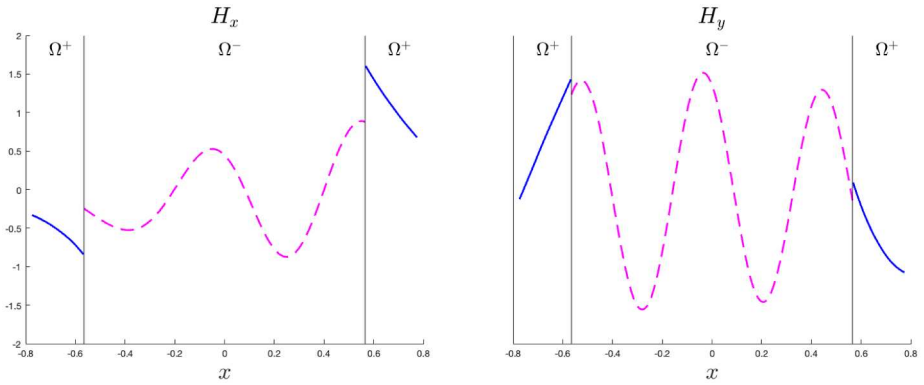

Fig. 28. The components H_x and H_y at $y = 0.2$ and the final time $t_f = 1$ for the scattering of a magnetic dielectric problem using the fifth-order Hermite-Taylor correction function method and $h = \frac{1}{460}$. The interface is represented by the vertical black line. The numerical solution in Ω^+ and Ω^- are respectively represented by the blue line and the dashed magenta line. (For interpretation of the references to colour in this figure legend, the reader is referred to the web version of this article.)

extrapolation procedure pointwise with $h = \frac{1}{800}$ and $h = \frac{1}{1600}$, and the fifth-order Hermite-Taylor correction function method. This leads to reference solution with at least a sixth-order accuracy. The reference solution is illustrated in Fig. 29. Afterward, we estimate the relative errors by comparing the reference solution to approximations coming from meshes with $h \in \{\frac{1}{50}, \frac{1}{100}, \frac{1}{200}, \frac{1}{400}, \frac{1}{800}\}$. Note that all primal nodes for these meshes are also part of the reference solution mesh. The relative error in the L^2-norm is computed at the final time. The left plot of Fig. 30 illustrates that we obtain the expected $2m+1$ rates of convergence. The $2m$ rates of convergence of the divergence of the magnetic field are illustrated in the left plot of Fig. 31.

We now consider the same geometry where we enforce PEC boundary conditions on Γ_1. The initial conditions are $H_x = H_y = 0$ and

$$E_z(x,y) = e^{\frac{-(x-0.5)^2-(y-0.5)^2}{2\sigma^2}}. \tag{61}$$

Here $\sigma = 0.01$. In this situation, we are not aware of an analytical solution. We then perform self convergence studies using the reference solution, illustrated in Fig. 32, that was computed using a Richardson procedure with $h = \frac{1}{800}$ and $h = \frac{1}{1600}$, and the fifth-order Hermite-Taylor correction function method. The right plot of Fig. 30 illustrates the self convergence plots in the L^2-norm. We obtain the expected $2m+1$ rates of convergence. The right plot of Fig. 31 shows the $2m$ rates of convergence of the divergence of the magnetic field.

5.2.4. *Increasing the order of the interior method*

As a final example, we increase the order of the interior method, here the Hermite-Taylor method. This could be advantageous in cases where waves propagate many wavelengths in the interior domain. This is possible since we can compute the derivatives through order k when correction function polynomials of degree k are used, allowing a Hermite-Taylor method with $m \leq k$. Although it is not used here, note that, for localized pulses, the p-adaptive algorithm introduced in [33] could be used for the interior method, far away from the boundary. Then, although the extent to which the order can be increased adjacent to the boundary is limited, there would be no fundamental limits to the order achieved far from the boundaries. We denote a Hermite-Taylor correction function method

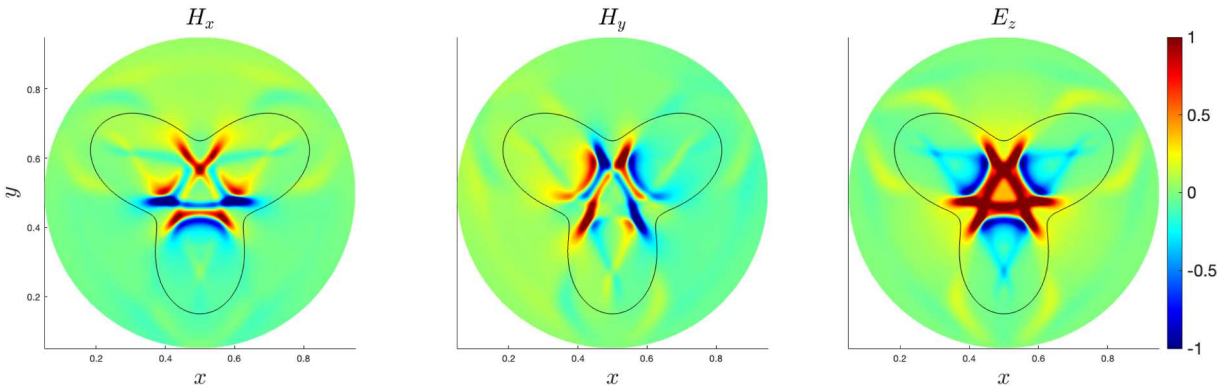

Fig. 29. The components H_x, H_y and E_z at the final time $t_f = 1$ for an interface problem with the geometry illustrated in Fig. 20 using the fifth-order Hermite-Taylor correction function method and $h = \frac{1}{1600}$. We consider a Gaussian pulse in time as the boundary condition for E_z. The interface is represented by the black line.

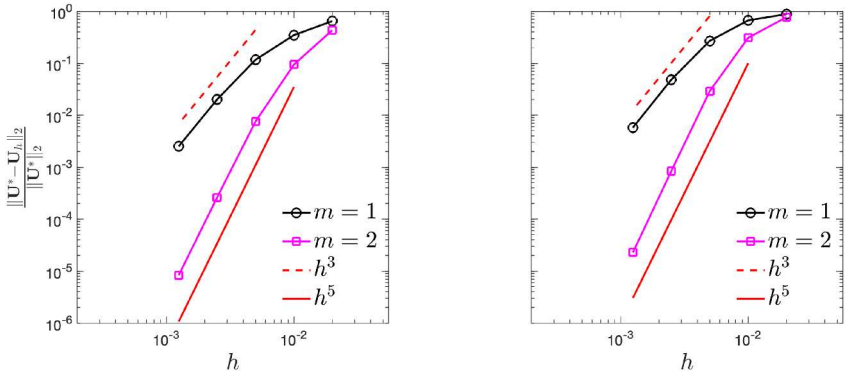

Fig. 30. Self convergence plots for interface problems with the geometry illustrated in Fig. 20 using the third and fifth order Hermite-Taylor correction function methods. For the left plot, we consider a Gaussian pulse in time as the boundary condition for E_z. For the right plot, we consider a Gaussian pulse as an initial condition for E_z. Here $\mathbf{U} = [H_x, H_y, E_z]^T$.

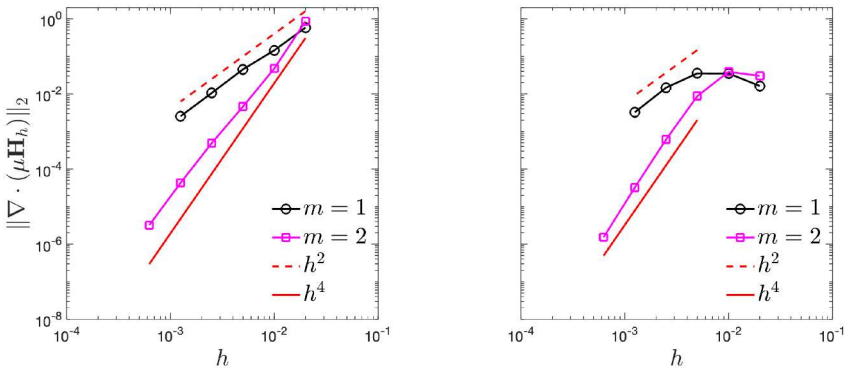

Fig. 31. Self convergence plots of the divergence of the magnetic field for interface problems with the geometry illustrated in Fig. 20 using the third and fifth order Hermite-Taylor correction function methods. For the left plot, we consider a Gaussian pulse in time as the boundary condition for E_z. For the right plot, we consider a Gaussian pulse as an initial condition for E_z.

that uses derivatives through order m and correction function polynomials of degree k as a (k, m)-method, leading to a $(k+1)$-order method near the boundary and $(2m+1)$-order method in the interior. Here we consider the situation when $k/2 \le m \le k$ with $k = 2 - 4$. We set $N_d = k$.

We first perform long time simulations with $h = 1/20$ using the same setup as for the embedded boundary problems. According to the results in Section 5.2.1, the $(2, 1)$ and $(4, 2)$ methods are numerically stable for respectively a CFL constant smaller than 1 and

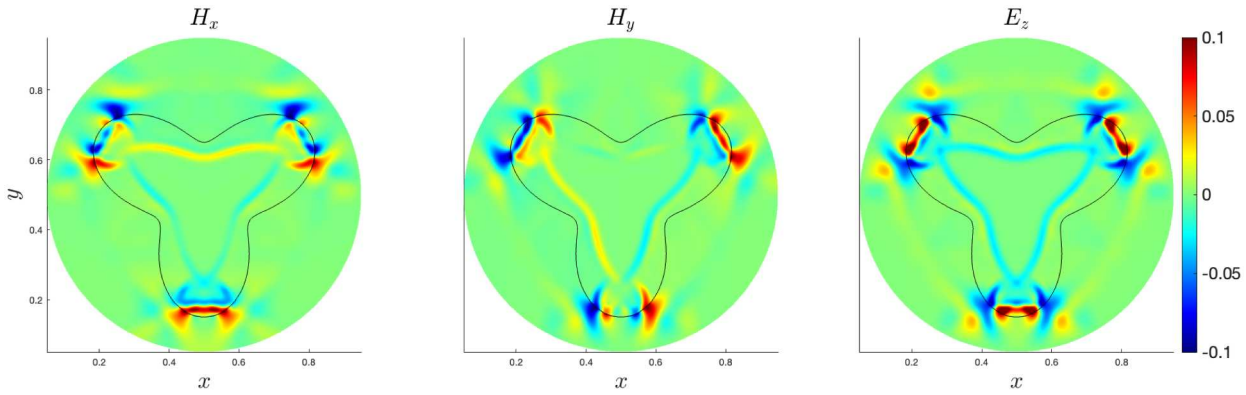

Fig. 32. The components H_x, H_y and E_z at the final time $t_f = 1$ for an interface problem with the geometry illustrated in Fig. 20 using the fifth-order Hermite-Taylor correction function method and $h = \frac{1}{1600}$. We consider a Gaussian pulse as an initial condition for E_z. The interface is represented by the black line.

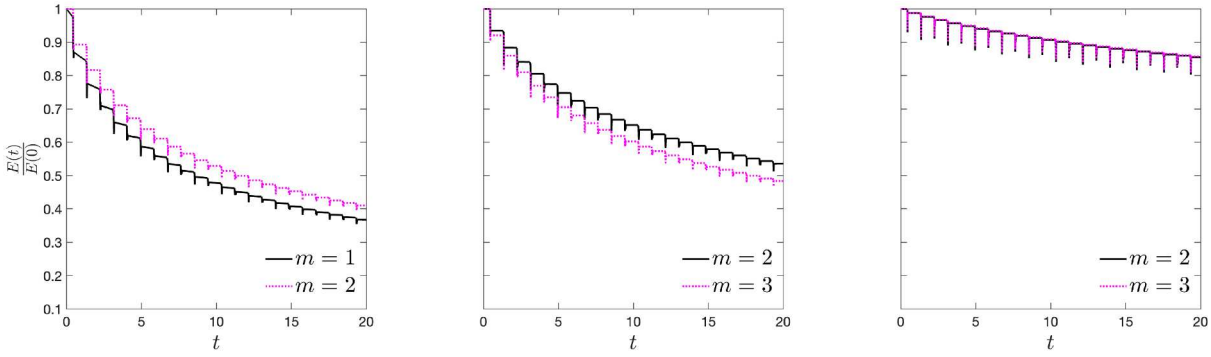

Fig. 33. The evolution of the energy as a function of time for different (k, m) methods. The left, middle and right plots are for respectively $k = 2$, $k = 3$ and $k = 4$.

0.8. For the remaining methods, we observe that the $(2, 2)$, $(3, 2)$, $(3, 3)$ and $(4, 3)$ methods are stable under a CFL constant smaller than 0.9, 1, 0.5 and 0.6, while the $(4, 4)$-method is unstable.

We now consider the computational domain $\Omega_c = [0, 1] \times [0, 1]$. The embedded boundary Γ is a circle with a radius of 0.45 and centered at $(0.5, 0.5)$ that encloses the physical domain Ω. We enforce PEC boundary conditions on the boundary Γ and consider the initial conditions $H_x = H_y = 0$ and E_z is given by (61). The physical parameters are $\mu = 1$ and $\epsilon = 1$. The CFL constant are 0.9, 0.85, 0.9, 0.45, 0.75 and 0.55 for respectively $(2, 1)$, $(2, 2)$, $(3, 2)$, $(3, 3)$, $(4, 2)$ and $(4, 3)$ methods. We investigate the energy conservation on the time interval $I = [0, 20]$ with $h = \Delta x = \Delta y = 1/200$. The energy at time t is

$$E(t) = \int_{\Omega} \epsilon \|\boldsymbol{E}(\boldsymbol{x}, t)\|_2^2 + \mu \|\boldsymbol{H}(\boldsymbol{x}, t)\|_2^2 \, \mathrm{d}\boldsymbol{x}. \tag{62}$$

Fig. 33 illustrates the evolution in time of the ratio $E(t)/E(0)$ for different (k, m) methods. Based on these results, the energy dissipates as the time increases, demonstrating the stability of these methods. As the degree k of the correction functions increases, the energy is better conserved as expected. The decay in the energy due to the interior method for $m = 2 - 3$ is negligible. In all the cases, the decay in the energy is mainly due to the correction function method when the waves interact with the boundary, representing by a sharp drop of the energy in Fig. 33.

6. Conclusion

In this work, we have proposed a novel Hermite-Taylor correction function method to handle embedded boundary and interface conditions for Maxwell's equations. We take advantage of the correction function method to update the numerical solution at the nodes where the Hermite-Taylor method cannot be applied. To do so, we minimize a functional that is a square measure of the residual of Maxwell's equations, the boundary or interface conditions, and the polynomials approximating the electromagnetic fields coming from the Hermite-Taylor method. The stability condition of the Hermite-Taylor correction function method is improved by enforcing the time derivatives, converted into spatial derivatives, of the boundary and interface conditions. The approximations of the electromagnetic fields and their required derivatives are then updated using the correction functions resulting from the minimization

procedure. For the embedded boundary problem in one space dimension, we were able to achieve up to a ninth-order rate of convergence and the methods are stable under a CFL constant between 0.7 and 1. In two space dimensions, numerical examples suggest that the third and fifth order Hermite-Taylor correction function methods are stable under a CFL constant of 1 and 0.8 respectively. The range of m that can be used and therefore the order of the overall method are limited by the large condition number of the CF matrices coming from the minimization problem when $m > 2$ in the multi-dimensional case. Note that we were able to increase the order of the interior method, here the Hermite-Taylor method, up to seven without significantly impacting the CFL constant. The accuracy of the Hermite-Taylor correction function method was verified. The proposed method achieves high order accuracy even with interface problems with discontinuous solutions. Finally, this method can be easily adapted to other first order hyperbolic problems.

CRediT authorship contribution statement

Yann-Meing Law: Writing - original draft, Visualization, Software, Methodology, Investigation, Formal analysis, Conceptualization; **Daniel Appelö:** Writing - review & editing, Methodology, Investigation, Formal analysis, Conceptualization; **Thomas Hagstrom:** Writing - review & editing, Methodology, Investigation, Formal analysis, Conceptualization.

Data availability

Data will be made available on request.

Declaration of competing interest

The authors declare that they have no known competing financial interests or personal relationships that could have appeared to influence the work reported in this paper.

Acknowledgments

This work was supported in part by NSF Grants DMS-2208164, DMS-2210286 and DMS-2012296. Any opinions, findings, and conclusions or recommendations expressed in this material are those of the authors and do not necessarily reflect the views of the NSF.

References

[1] J.S. Hesthaven, High-order accurate methods in time-domain computational electromagnetics: a review, Adv. Imag. Electron Phys. 127 (2003) 59–123.
[2] A. Ditkowski, K. Dridi, J.S. Hesthaven, Convergent Cartesian grid methods for Maxwell equations in complex geometries, J. Comput. Phys. 170 (2001) 39–80.
[3] W. Cai, S. Deng, An upwinding embedded boundary method for Maxwell's equations in media with material interfaces: 2D case, J. Comput. Phys. 190 (2003) 159–183.
[4] S. Zhao, G.W. Wei, High-order FDTD methods via derivative matching for Maxwell's equations with material interfaces, J. Comput. Phys. 200 (2004) 60–103.
[5] Y. Zhang, D.D. Nguyen, K. Du, J. Xu, S. Zhao, Time-domain numerical solutions of Maxwell interface problems with discontinuous electromagnetic waves, Adv. Appl. Math. Mech. 8 (2016) 353–385.
[6] J.W. Banks, B.B. Buckner, W.D. Henshaw, M.J. Jenkinson, A.V. Kildishev, G. Kovačič, L.J. Prokopeva, D.W. Schwendeman, A high-order accurate scheme for Maxwell's equations with a generalized dispersive material (GDM) model and material interfaces, J. Comput. Phys. 412 (2020) 109424.
[7] Y.M. Law, J.C. Nave, High-order FDTD schemes for Maxwell's interface problems with discontinuous coefficients and complex interfaces based on the correction function method, J. Sci. Comput. 91 (1) (2022) 26.
[8] B. Cockburn, C.W. Shu, Runge–Kutta discontinuous Galerkin methods for convection-dominated problems, J. Sci. Comput. 16 (3) (2001) 173–261.
[9] J.S. Hesthaven, T. Warburton, Nodal high-order methods on unstructured grids: I. time-domain solution of Maxwell's equations, J. Comput. Phys. 181 (2002) 186–221.
[10] B. Yang, D. Gottlieb, J.S. Hesthaven, Spectral simulations of electromagnetic wave scattering, J. Comput. Phys. 134 (1997) 216–230.
[11] T.A. Driscoll, B. Fornberg, Block pseudospectral methods for Maxwell's equations II: two-dimensional, discontinuous-coefficient case, SIAM J. Sci. Comput. 21 (1999) 1146–1167.
[12] G.-X. Fan, Q.H. Liu, J.S. Hesthaven, Multidomain pseudospectral time-domain simulations of scattering by objects buried in lossy media, IEEE Trans. Geosci. Remote Sens. 40 (2002) 1366–1373.
[13] R. Galagusz, D. Shirokoff, J.C. Nave, A Fourier penalty method for solving the time-dependent Maxwell's equations in domains with curved boundaries, J. Comput. Phys. 306 (2016) 167–198.
[14] J. Goodrich, T. Hagstrom, J. Lorenz, Hermite methods for hyperbolic initial-boundary value problems, Math. Comp. 75 (2005) 595–630.
[15] W. Chen, X. Li, D. Liang, Energy-conserved splitting finite-difference time-domain methods for Maxwell's equations in three dimensions, SIAM J. Numer. Anal. 48 (2010) 1530–1554.
[16] O. Beznosov, D. Appelö, Hermite - discontinuous Galerkin overset grid methods for the scalar wave equation, Commun. Appl. Math. Comput. (2020).
[17] A.A. Loya, D. Appelö, W.D. Henshaw, High order accurate Hermite schemes on curvilinear grids with compatibility boundary conditions, J. Comput. Phys. 522 (2025) 113597.
[18] Y.-M. Law, D. Appelö, The Hermite-Taylor correction function method for Maxwell's equations, Commun. Appl. Math. Comput. (2023). https://doi.org/10.1007/s42967-023-00287-5
[19] A.N. Marques, J.-C. Nave, R.R. Rosales, A correction function method for Poisson problems with interface jump conditions, J. Comput. Phys. 230 (2011) 7567–7597.
[20] A.N. Marques, J.-C. Nave, R.R. Rosales, High order solution of Poisson problems with piecewise constant coefficients and interface jumps, J. Comput. Phys. 335 (2017) 497–515.
[21] D.S. Abraham, A.N. Marques, J.C. Nave, A correction function method for the wave equation with interface jump conditions, J. Comput. Phys. 353 (2018) 281–299.
[22] Y.-M. Law, A.N. Marques, J.C. Nave, Treatment of complex interfaces for Maxwell's equations with continuous coefficients using the correction function method, J. Sci. Comput. 82 (3) (2020) 56.

[23] Y.M. Law, J.C. Nave, FDTD schemes for Maxwell's equations with embedded perfect electric conductors based on the correction function method, J. Sci. Comput. 88 (3) (2021) 72.
[24] F. Assous, P. Ciarlet, S. Labrunie, Mathematical Foundations of Computational Electromagnetism, Springer International Publishing, 2018.
[25] W.D. Henshaw, H.-O. Kreiss, L.G.M. Reyna, A fourth-order-accurate difference approximation for the incompressible Navier-Stokes equations, Comput. Fluids 23 (1994) 575–593.
[26] S. Tan, C.W. Shu, Inverse Lax-Wendroff procedure for numerical boundary conditions of conservation laws, J. Comput. Phys. 229 (21) (2010) 8144 – 8166.
[27] D. Appelö, J.W. Banks, W.D. Henshaw, D.W. Schwendeman, Numerical methods for solid mechanics on overlapping grids: linear elasticity, J. Comput. Phys. 231 (2012) 6012–6050.
[28] W.D. Henshaw, A high-order accurate parallel solver for Maxwell's equations on overlapping grids, SIAM J. Sci. Comput. 28 (5) (2006) 1730–1765.
[29] J.B. Angel, J.W. Banks, W.D. Henshaw, M.J. Jenkinson, A.V. Kilidishev, G.K. L. J. Prokopeva, D.W. Schwendeman, A high-order accurate scheme for Maxwell's equations with a generalized dispersive material model, J. Comput. Phys. 378 (2019) 441–444.
[30] D.S. Abraham, D.D. Giannacopoulos, A parallel implementation of the correction function method for Poisson's equation with immersed surface charges, IEEE Trans. Magn. 53 (6) (2017).
[31] H. Zhou, W. Ying, A correction function-based kernel-free boundary integral method for elliptic PDEs with implicitly defined interfaces, J. Comput. Phys. 496 (2024) 112545.
[32] A. Taflove, Computational Electrodynamics: The Finite Difference Time-Domain Method, Artech House, 1995.
[33] R. Chen, T. Hagstrom, *P*-adaptive Hermite methods for initial value problems, ESAIM: M2AN 46 (2012) 545–557.